The SWELLS survey. IV. Precision measurements of the stellar and dark matter distributions in a spiral lens galaxy

Matteo Barnabè,[1]★ Aaron A. Dutton,[2,3,4]† Philip J. Marshall,[5] Matthew W. Auger,[2,6]
Brendon J. Brewer,[2] Tommaso Treu,[2]‡ Adam S. Bolton,[7] David C. Koo[3]
and Léon V. E. Koopmans[8]

[1]*Kavli Institute for Particle Astrophysics and Cosmology, Stanford University, 452 Lomita Mall, Stanford, CA 94035, USA*
[2]*Dept. of Physics, University of California, Santa Barbara, CA 93106, USA*
[3]*UCO/Lick Observatory, Department of Astronomy and Astrophysics, University of California, Santa Cruz, CA 95064, USA*
[4]*Dept. of Physics and Astronomy, University of Victoria, Victoria, BC, V8P 5C2, Canada*
[5]*Department of Physics, University of Oxford, Keble Road, Oxford, OX1 3RH, UK*
[6]*Institute of Astronomy, University of Cambridge, Madingley Rd, Cambridge, CB3 0HA, UK*
[7]*Department of Physics and Astronomy, University of Utah, Salt Lake City, UT 84112, USA*
[8]*Kapteyn Astronomical Institute, University of Groningen, P.O.Box 800, 9700 AV Groningen, The Netherlands*

ABSTRACT

We construct a fully self-consistent mass model for the lens galaxy SDSS J2141 at redshift 0.14, and use it to improve on previous studies by modelling its gravitational lensing effect, gas rotation curve and stellar kinematics simultaneously. We adopt a very flexible axisymmetric mass model constituted by a generalized NFW dark matter halo and a stellar mass distribution obtained by deprojecting the multi-Gaussian expansion (MGE) fit to the high-resolution K'-band Laser Guide Star Adaptive Optics (LGSAO) imaging data of the galaxy, with the (spatially constant) mass-to-light ratio as a free parameter. We model the stellar kinematics by solving the anisotropic Jeans equations. We find that the inner logarithmic slope of the dark halo is weakly constrained, i.e. $\gamma = 0.82^{+0.65}_{-0.54}$, and consistent with an unmodified NFW profile; we can conclude, however, that steep profiles ($\gamma \geqslant 1.5$) are disfavoured ($< 14\%$ posterior probability). We marginalize over this parameter to infer the galaxy to have (i) a dark matter fraction within 2.2 disk radii of $0.28^{+0.15}_{-0.10}$, independent of the galaxy stellar population, implying a maximal disk for SDSS J2141; (ii) an apparently uncontracted dark matter halo, with concentration $c_{-2} = 7.7^{+4.2}_{-2.5}$ and virial velocity $v_{\rm vir} = 242^{+44}_{-39}$ km s^{-1}, consistent with ΛCDM predictions; (iii) a slightly oblate halo ($q_h = 0.75^{+0.27}_{-0.16}$), consistent with predictions from baryon-affected models. Comparing the tightly constrained gravitational stellar mass inferred from the combined analysis ($\log_{10} M_\star/M_\odot = 11.12^{+0.05}_{-0.09}$) with that inferred from stellar populations modelling of the galaxies colours, and accounting for an expected cold gas fraction of 20 ± 10 per cent, we determine a preference for a Chabrier IMF over Salpeter IMF by a Bayes factor of 5.7 (corresponding to substantial evidence). We infer a value $\beta_z \equiv 1 - \sigma_z^2/\sigma_R^2 = 0.43^{+0.08}_{-0.11}$ for the orbital anisotropy parameter in the meridional plane, in agreement with most studies of local disk galaxies, and ruling out at 99 per cent confidence level that the dynamics of this system can be described by a two-integral distribution function.

Key words: gravitational lensing: strong — galaxies: fundamental parameters — galaxies: haloes — galaxies: kinematics and dynamics — galaxies: spiral — galaxies: structure

★ mbarnabe@stanford.edu
† CITA National Fellow
‡ Packard Research Fellow

1 INTRODUCTION

Measuring the relative contribution of luminous and dark matter in spiral galaxies is essential to understand their internal structure and therefore constrain the physical processes that drive their formation and evolution (e.g. Dutton et al. 2011a). Traditionally this is done by means of detailed stellar and gas kinematics and stellar population diagnostics (e.g. Bershady et al. 2011). However, often one needs additional assumptions about the relative contribution of the stars and dark matter (e.g. van Albada & Sancisi 1986), or about the stellar initial mass function (e.g. Bell & de Jong 2001).

The combination of strong gravitational lensing and galaxy kinematics is a powerful tool for constraining the mass distribution and the dynamical structure of galaxies beyond the local Universe, since this approach makes it possible to overcome many of the difficulties associated with the traditional techniques, which are severely limited when applied to distant objects (see e.g. Treu & Koopmans 2002, 2004; Barnabè & Koopmans 2007; Jiang & Kochanek 2007; Grillo et al. 2008; Auger et al. 2010a; Koopmans et al. 2009; Barnabè et al. 2010, 2011). In particular, gravitational lenses in which the deflector contains a high inclination disk provide extra (geometrical) information to help disentangle the distribution of baryons and dark matter, and to measure the 3D shape of the dark matter halo (e.g., Keeton & Kochanek 1998, Koopmans et al. 1998, Maller et al. 2000, Trott et al. 2010, Suyu et al. 2011 and Dutton et al. 2011b, Paper II of this series) Because these measured masses are gravitational, they can be compared with the stellar mass from stellar population synthesis (SPS) models and so used to constrain the form of the stellar initial mass function (IMF), and the response of dark matter haloes to galaxy formation.

Until recently only a small number of gravitational lenses with high-inclination disks were known. The SLACS (Bolton et al. 2006, 2008) and SWELLS (Treu et al. 2011, Paper I) surveys have significantly increased the number of known gravitational lenses in which the deflector contains a high-inclination disk, including several disk-dominated systems.

One of the most promising spiral lens systems for a joint lensing and dynamics analysis is SDSS J2141−0001 (hereafter simply referred to as SDSS J2141 for brevity), at redshift $z_{lens} = 0.1380$, which is a disk-dominated galaxy (it has a disk K'-band light fraction of $\simeq 80\%$) at high inclination ($i \simeq 78°$). In addition to the discovery data from the SLACS survey, a wealth of imaging and kinematic data are available from the SWELLS project (Paper I and II). A joint strong lensing and gas kinematics (rotation curve) analysis of SDSS J2141 conducted in Paper II yielded a gravitational stellar mass of $\log_{10}(M_\star/M_\odot) = 10.99^{+0.11}_{-0.25}$ (consistent with that from a stellar population analysis assuming a Chabrier IMF), a dark matter fraction at 2.2 disk scale lengths of $f_{DM} = 0.55^{+0.20}_{-0.15}$, and a dark matter halo flattening of $q_h = 0.91^{+0.15}_{-0.13}$. However, in that work, simple phenomenological ("Chameleon") models for all three mass components, i.e. the dark matter halo and the stellar bulge and disk, were assumed. Moreover, only a fraction of the available kinematic data for the lens galaxy was used: the stellar velocity dispersion and rotation curve were not considered. Indeed, the velocity dispersion could not be predicted self-consistently within the assumed model.

In this paper we improve on the Paper II analysis of SDSS J2141 in several important ways. The main improvement is the inclusion of stellar kinematics data, which provides a mass constraint at smaller radii than obtained from lensing or gas kinematics. It is well known that disk galaxies are usually characterized by a velocity dispersion ellipsoid flattened along the vertical direc-

tion: therefore, in order to provide an accurate description of the data set, we model the stellar kinematics by means of anisotropic Jeans equations, which allow us to properly take into account (and recover) the anisotropy ratio parameter β_z. In addition to this, we use more flexible and general models for both the stellar and the dark matter density profiles. Specifically, we obtain the stellar mass density profile from the deprojection of the observed luminous distribution (fitted with the state-of-the-art method of multi-Gaussian expansion, MGE, see Cappellari 2002), rather than the sum of two "Chameleon" profiles, which were used to approximate a Sérsic profile bulge (Sérsic 1968) and an exponential disk. Finally, here we model the dark matter halo with an ellipsoidal generalized NFW profile (inner logarithmic slope $-\gamma$, outer slope -3) rather than the non-singular isothermal ellipsoid (inner slope 0, outer slope -2) with a fixed density profile in the inner regions used in the previous analysis.

The resulting model is both self-consistent and, in the case of the dark matter halo, physically-motivated, and allows us to attempt to fit all the data we have for SDSS J2141 simultaneously. We use it to answer the following questions about SDSS J2141: How much does dark matter contribute to the total mass of this disk galaxy, in particular in the inner regions? What is the concentration and inner profile slope of its dark matter halo? What is its halo's shape? When calibrated via its stellar mass distribution's gravitational effects, what galaxy-averaged IMF do we infer from a stellar population synthesis analysis of its optical and near infra-red colours? What is the vertical-to-radial anisotropy of its velocity dispersion ellipsoid?

This paper is structured as follows. We first describe our observational data (imaging for the lens modelling, spectroscopy for the stellar and gas kinematics) in Section 2. We then outline our mass model for SDSS J2141 in Section 3, giving the functional forms we use to describe its stellar and dark matter distributions. Then, in Section 4 and Section 5 we show how our model predicts both the lensing and kinematic data in a self-consistent way, and in Section 6 we review the probability theory behind the actual inference procedure we follow. In Section 7 we present and discuss the results of our analysis, and in Section 8 we draw conclusions, providing an answer to the questions posed above.

Throughout this work, we assume a flat ΛCDM cosmology with present day matter density, $\Omega_m = 0.3$, and Hubble parameter, $H_0 = 70 \, km \, s^{-1} \, Mpc$.

2 OBSERVATIONS

In this Section we briefly recall the data set available for this study. A more detailed description of the data is given in Paper II.

2.1 Imaging data

The imaging data consists of a high spatial resolution (FWHM $\simeq 0.15$ arcsec) K'-band image taken with adaptive optics on the Keck II telescope. The galaxy-subtracted image (see Paper II) is used for the strong lensing analysis, while the light profile of the galaxy is fitted with a set of elliptical Gaussians which are deconvolved and deprojected to provide a 3D model of the stellar mass (up to the normalization), as detailed in Section 3.1. The lens-subtracted image used as data set for the lensing analysis is shown in the upper-right panel of Figure 1. Multi-band HST photometry is also available and used to determine stellar mass as discussed in Papers I and II.
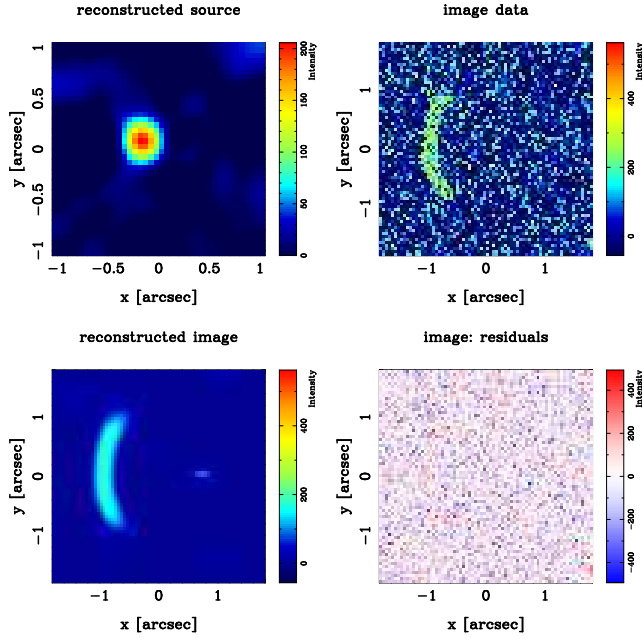
Figure 1. Lensed image reconstruction obtained from the *maximum a posteriori* model. From the top left-hand to bottom right-hand panel: reconstructed source; *HST*/ACS data showing the observed lensed image after subtraction of the lens galaxy; lensed image reconstruction corresponding to the source in the first panel; residuals.

2.2 Kinematic data

The second set of data that we will use to constrain our mass model is the rotation and velocity dispersion profiles derived from optical emission- and absorption-line spectroscopy. A major axis long-slit spectrum of SDSS J2141 was obtained with the DEep Imaging Multi-Object Spectrograph (DEIMOS) on the Keck II 10-m telescope.

We used the 1200 line grating (corresponding to a pixel scale of 0.32 Å) with a 1 arcsec width slit resulting in a spectral resolution of $\sim$ 1.9 Å. The wavelength range was $5200 - 7800$ Å, covering several prominent emission and absorption lines. At the wavelength of Mgb the velocity resolution is $\sigma_{res} \simeq 41$ km s^{-1}, and for Hα it is $\sigma_{res} \simeq 32$ km s^{-1}. We took three exposures of 1200s in excellent seeing conditions of 0.60 arcsec. The spectra were reduced using routines developed by D. Kelson (Kelson 2003).

Kinematic parameters were measured from one-dimensional spectra extracted along the slit with a spatial sampling of $\simeq$ 0.59 arcsec (5 DEIMOS pixels), corresponding to one data point per seeing FWHM. The rotation and velocity dispersion profile of the stars were obtained by fitting a region including the Mgb [5177 Å] and FeII [5270 Å] lines with a set of stellar templates.

The rotation curve of the ionized gas was measured by fitting Gaussians to the Hα line [6563 Å], and is shown in the upper panel of Figure 2 (data points with error bars). Outside of the inner $\sim$ 2 arcsec the velocity dispersion of the Hα line was equal to the instrumental resolution, indicating the ionized gas disk is dynamically cold.

In our dynamical model (see Section 5), we assume that the ionized gas traces the circular velocity of the galaxy (i.e., there is no pressure support). For the stellar kinematics our model implicitly includes rotation and dispersion, although neither of these parameters are fitted to directly. Instead, our model predicts the projected second velocity moment, which is fitted to the root mean square
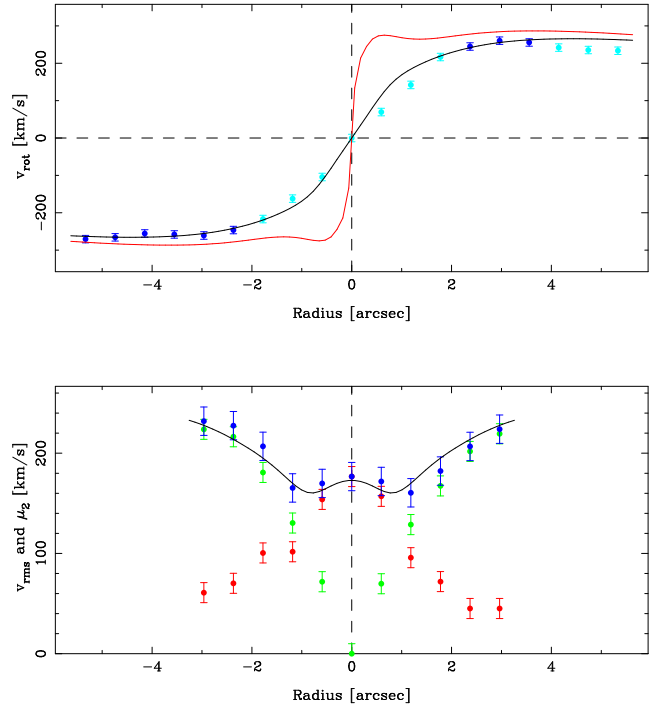
Figure 2. Observed gas and stellar kinematics compared to the predictions of the *maximum a posteriori* model. The *upper panel* shows the galaxy Hα rotation curve (blue data points): the red line represents the intrinsic model circular velocity, while the black line gives the predicted observable, i.e. the model circular velocity after the beam-smearing, finite slit width and inclination effects are taken into account. The light blue data points are not used to constrain the model (see text). The *lower panel* shows the model projected second velocity moment μ_2 (black line) compared to the corresponding observational quantity v_{rms} (blue data points). The stellar kinematic data sets $|v_{rot}|$ (stellar rotation curve, green) and σ (stellar velocity dispersion profile, red) are also shown for reference. See Section 5 for a rigorous definition of these quantities.

velocity of the stars, $v_{rms}(R) = \sqrt{v_{rot}^2(R) + \sigma^2(R)}$ (see Cappellari 2008). The lower panel of Figure 2 shows the observables v_{rot} and σ (as green and red data points, respectively) as well as the root mean square velocity (blue data points).

In our modelling, as described in Paper II, we conservatively exclude from the fit the data points of the gas rotation curve that are (i) within the inner 2 arcsec (due to uncertainties and likely asymmetries in the Hα distribution in this region) and (ii) beyond 3.5 arcsec on the west side of the rotation curve (where there is an asymmetry caused by the presence of the warp). These excluded points are shown in light blue in Figure 2.

3 THE GALAXY MASS MODEL

In order to perform a self-consistent analysis of the mass structure of SDSS J2141 we need to combine the constraints derived from both the lensing and kinematics data sets. The most general and straightforward way to proceed is simply to adopt for the galaxy a plausible total mass density distribution $\rho_{tot}(\boldsymbol{x}, \boldsymbol{\eta})$, where $\boldsymbol{x}$ denotes the spatial coordinates and $\boldsymbol{\eta}$ is a set of parameters characterizing the density profile, and use it to model simultaneously the various sets of observables. The main challenge with this approach lies in choosing a mass distribution that is realistic and flexible enough to reproduce the data, but at the same time simple enough that the

exploration of the η parameter space remains computationally feasible.

In keeping with local studies of both disk and elliptical galaxies (e.g. Weijmans et al. 2008, Williams et al. 2009) we model the mass distribution using two components: (i) a luminous mass component whose detailed profile is obtained by deprojecting the observed surface brightness distribution and (ii) a generalized NFW dark matter halo whose profile is motivated by cosmological simulations.

Throughout the remainder of this work we will make reference to the two following right-handed coordinate systems: (i) a cylindrical coordinate system (R, φ, z) with the z-axis directed along the galaxy rotation axis; (ii) a Cartesian coordinate system (x', y', z'), where the z'-axis is directed along the line-of-sight and (x', y') denotes the plane of the sky, with the x'-axis aligned along the galaxy projected major axis. In both cases the origin of the axes is located in the center of the galaxy (which is assumed to be an axially symmetric system). We use the first reference system to write the intrinsic galactic quantities (e.g. density and potential) and the second one to express the projected quantities (e.g. surface brightness and deflection angle). We denote with i the galaxy inclination, i.e. the angle comprised between the z- and z'-axes (so that $i = 90°$ for a system observed edge-on).

3.1 Luminous mass distribution

An ideal model for the luminous mass distribution should be flexible and realistic (in particular, it should be able to reproduce the observed surface brightness distributions when projected along the line-of-sight), and analytically simple, so that the corresponding gravitational potential is easy to calculate. This can be achieved by making use of the MGE method, a technique originally pioneered by Bendinelli (1991) and subsequently generalized and developed by Monnet, Bacon, & Emsellem (1992), Emsellem, Monnet, & Bacon (1994), Emsellem, Dejonghe, & Bacon (1999) and Cappellari (2002), whose formalism we follow here. In order to minimize dust obscuration and map as closely as possible the stellar distribution, we apply the MGE decomposition to the high-resolution K'-band image of the SDSS J2141 surface brightness distribution.

The observed galaxy surface brightness $\Sigma(x', y')$ is parametrized as a sum of N two-dimensional, concentric, elliptically-symmetric Gaussian components $g_k(x', y')$, each with luminosity L_k:

$$\Sigma(x', y') = \sum_k L_k \, g_k(x', y') \,, \tag{1}$$

where each Gaussian function

$$g_k(x', y') = \frac{1}{2\pi\sigma_k^2 q_k'} \exp\left[-\frac{1}{2\sigma_k^2}\left(x'^2 + \frac{y'^2}{q_k'^2}\right)\right] \tag{2}$$

is characterized by the widths σ_k and $q_k'\sigma_k$ along the x'- and y'-axis respectively, and q_k' is the projected axial ratio of the k-th component. The total stellar luminosity of the system is simply given by $L_{\text{tot}} = \sum_k L_k$.

In general, even assuming — as we do — that the galaxy inclination angle i is known, the deprojection of the observed light distribution of an axisymmetric galaxy is an intrinsically degenerate problem unless the system is seen edge-on (Rybicki 1987). The solution, however, can become unique when a model is specified. In the case of the MGE parametrization, the deprojected three-

dimensional luminosity density distribution has the simple expression

$$\rho(R, z) = \sum_k \frac{L_k}{(2\pi)^{3/2}\sigma_k^3 q_k} \exp\left[-\frac{1}{2\sigma_k^2}\left(R^2 + \frac{z^2}{q_k^2}\right)\right], \tag{3}$$

which is still a sum of Gaussian functions with intrinsic axial ratios given by

$$q_k^2 = \frac{q_k'^2 - \cos^2 i}{\sin^2 i} \,. \tag{4}$$

Since the stellar component of galaxies is oblate or spherical, most (if not all) Gaussians will turn out to have $0 \leqslant q_k \leqslant 1$. In order for the axial ratios of the 3D Gaussian components to be physical, one must enforce the constraint that the projected axial ratios q_k' are rounder than $|\cos i|$ when fitting the profile of Eq. (1) to the observed surface brightness distribution.

The luminosity density in Eq. (3) can be straightforwardly converted into a mass density by multiplying each term by the stellar mass-to-light ratio Υ_k, so that the mass of each Gaussian is given by $M_k \equiv \Upsilon_k L_k$. However, the single Gaussian elements are simply a mathematically convenient way to describe the light profile and do not have a direct physical meaning individually. Therefore, since there is little interest in studying them one by one, in this work we assign the same global stellar mass-to-light ratio $\Upsilon_\star$ to all the luminous components. This simplifying assumption is equivalent to assuming that the bulge and disk components have the same stellar mass-to-light ratio. Note that the choice of the K'-band image as trace of stellar light should minimize variations in mass-to-light ratio. Future work with higher resolution data should explore further the limitations of this assumption.

An additional advantage of the MGE approach is that we avoid dealing with the difficult and somewhat degenerate problem of decomposing the light profile into the separate disk and bulge contributions (see e.g. van der Kruit & Searle 1981) since we have a model that can fit very accurately the whole light distribution at once.

The density distribution of Eq. (3) is a sum of components stratified on homoeoidal surfaces, hence the corresponding gravitational potential can be derived using the classic Chandrasekhar (1969) formula, obtaining (see Emsellem et al. 1994)

$$\Phi(R, z) = -G\sqrt{\frac{2}{\pi}} \sum_k \frac{M_k}{\sigma_k} \tilde{\Phi}_k(R, z) \,, \tag{5}$$

where G is the gravitational constant and the dimensionless function

$$\tilde{\Phi}_k(R, z) = \int_0^1 \frac{d\tau}{\sqrt{1 - \eta_k^2\tau^2}} \exp\left[-\frac{\tau^2}{2\sigma_k^2}\left(R^2 + \frac{z^2}{1 - \eta_k^2\tau^2}\right)\right], \tag{6}$$

with $\eta_k^2 \equiv 1 - q_k^2$, can be evaluated with a single numerical integral. The density distribution (Eq. 3) and its potential (Eq. 5) are remarkably simple for such a flexible mass model. Even better, the corresponding kinematic quantities, obtained by solving the Jeans equations, also have relatively straightforward expressions that do not involve any special functions (see Cappellari 2008 for a rigorous derivation of the velocity moments).

3.2 Dark matter halo

Cold dark matter simulations are known to produce halos with, on average, universal mass density profiles (Navarro, Frenk, & White 1997, NFW) that are well fitted by a broken power-law functional

form with an inner logarithmic slope $\gamma = 1$ and a slope $\gamma = 3$ in the outer regions, i.e. at radial distances much larger than the scale radius r_s. The situation, however, becomes far more complex when the baryons are added to the picture and — although the detailed mechanisms are not yet fully understood — it is widely accepted that the involved processes can have the effect of modifying the inner slope of the dark halo density profile (e.g. Blumenthal et al. 1986; Dekel et al. 2003; Gnedin et al. 2004; Nipoti et al. 2004; Abadi et al. 2010). Therefore, in order to account for a dark matter halo that can be either steeper or shallower than a NFW in the inner regions, we adopt an axisymmetric generalized NFW (gNFW) density distribution (see Zhao 1996; Wyithe et al. 2001):

$$\rho_{\text{DM}}(m) = \frac{\delta_c \, \rho_{\text{crit}}}{(m/r_s)^\gamma \, (1 + m/r_s)^{3-\gamma}} \, . \tag{7}$$

Here, ρ_{crit} is the critical density of the universe at the redshift of the object in question, and m denotes the elliptical radius, i.e.

$$m^2 \equiv R^2 + \frac{z^2}{q_h^2}, \tag{8}$$

where q_h indicates the three-dimensional axial ratio of the profile (the halo is oblate for $q_h < 1$, spherical for $q_h = 1$, prolate for $q_h > 1$). Note that we take the halo to be aligned with the stellar mass distribution, as in Paper II.

In order to enable an easier comparison of the scale radii between profiles having different values of γ, it is useful to introduce the quantity $r_{-2} \equiv (2 - \gamma)r_s$, which corresponds to the radius at which the logarithmic density slope of the profile is -2. Clearly, $r_{-2} = r_s$ only in the case of the regular NFW profile. Another useful scale length is the "virial" radius r_{vir}, defined as the spherical radius within which the average density is equal to $200 \, \rho_{\text{crit}}$. The concentration parameter of the halo is usually expressed as the ratio $c = r_{\text{vir}}/r_s$; an alternative definition, adopting the radius r_{-2}, is $c_{-2} = r_{\text{vir}}/r_{-2}$.

The characteristic halo density δ_c that sets the normalization of ρ_{DM} in the center is then expressed (following, e.g., Dutton et al. 2005)[1] as a function of both the concentration and the slope:

$$\delta_c = \frac{200}{3} \frac{c^3}{\zeta(c, \gamma, 1)} \, , \tag{9}$$

where we have defined the function

$$\zeta(c, \gamma, q_h) = \int_0^c \frac{\tau^{2-\gamma}(1 + \tau)^{\gamma-3}}{\sqrt{1 - (1 - q_h^2)\tau^2/c^2}} \, d\tau \, . \tag{10}$$

The mass distribution given by Eq. (7) is completely specified when the four independent parameters γ, q_h, r_s and c are given. In this work, we choose to re-parametrize the halo using the virial velocity v_{vir}, i.e. the circular velocity at the virial radius, in place of the scale radius, since v_{vir} has a very intuitive physical interpretation and facilitates the comparison with theoretical work, where this quantity is frequently employed (see e.g. Macciò et al. 2008; Dutton et al. 2011a). If the velocity is expressed in km s^{-1} and the radii in kpc, then one can show (cf. Dutton et al. 2005) that v_{vir} is related to the virial radius by the formula

$$\left(\frac{v_{\text{vir}}}{r_{\text{vir}}}\right)^2 = h^2 \frac{\zeta(c, \gamma, q_h)}{\zeta(c, \gamma, 1)} \, , \tag{11}$$

---

[1] Note that there is a typographical error in Eq. (7) of Dutton et al. (2005): inside the integral the numerator should read $y^{2-\alpha}[1 + (2 - \alpha)y]^{\alpha-3}$.

where $h = H/100 \, \text{km s}^{-1} \, \text{Mpc}^{-1}$ and H denotes the value of the Hubble constant at the redshift of the object.

It is convenient to perform an MGE of the axisymmetric gNFW profile in order to simplify considerably both the calculation of the lensing angle and the solving of the Jeans equations (cf., e.g., Williams et al. 2009, where a MGE decomposition of the NFW halo is performed). We find that around 8 Gaussian components are typically enough to provide an excellent fit to both the ρ_{DM} distribution and the lensing deflection field (typically within 1-3 per cent), ensuring that the adoption of this approximation does not change our inferences. In this case, the total potential is still obtained from Eq. (5) by extending the sum to include also the N_{DM} Gaussian elements that describe the dark halo component.

4 MODELLING THE GRAVITATIONAL LENSING

Given the observed surface brightness distribution of the lensed images and a mass model for the deflector, we recover the unlensed surface brightness distribution of the background object (the "source" object) by making use of the pixellated source reconstruction method, which takes into account the effects of PSF blurring and regularization (see e.g. Warren & Dye 2003; Koopmans 2005; Suyu et al. 2006; Brewer & Lewis 2006). Our implementation of this method is described in detail in Barnabè & Koopmans (2007) and is included in the CAULDRON code that has been employed in the combined lensing and dynamics analysis of the SLACS early-type galaxies for which two-dimensional kinematic maps are available (see Czoske et al. 2008, 2012; Barnabè et al. 2009a, 2009b, 2011).

This approach consists in casting back, pixel by pixel, through the lensing equation, the lensed image grid onto the source image grid. The results of this procedure are encoded in the lensing operator **A**, which allows one to express the mapping of the background source s into the lensed image d as a linear problem, i.e. $\mathbf{A}s = d$. This set of linear equations is then solved for s by means of very efficient standard techniques.

All that is needed to calculate the lensing operator is the deflection angle α, which is obtained from the surface mass density distribution of the lens galaxy (see e.g. Schneider, Kochanek, & Wambsganss 2006). Therefore, the matrix **A** depends both on the physical parameters η characterizing the density profile and on the geometry of the system, i.e. the inclination i and the angular diameter distances between the observer and the source (D_s), between the observer and the lens (D_d), and between the lens and the source (D_{ds}).

For many three-dimensional density profiles of astrophysical interest the deflection angle is very cumbersome to compute (cf., e.g., the catalogue of Keeton 2001). This has contributed to the widespread adoption of those few profiles, such as the isothermal ellipsoid, for which analytical expressions of α are available (see Kormann, Schneider, & Bartelmann 1994; Keeton & Kochanek 1998). Remarkably, the lensing deflection angle corresponding to the density distribution of Eq. (3) is very straightforward to calculate, involving a single quadrature and no special functions:

$$\alpha_{x'}(x', y') = \frac{1}{\pi D_d^2 \Sigma_{\text{crit}}} \int_0^1 \tau \, d\tau \sum_k \frac{M_k}{\sigma_k} \frac{\tilde{x}'}{\sqrt{1 - \eta_k^2 \tau^2}}$$
$$\times \exp\left[-\frac{\tau^2}{2}\left(\tilde{x}'^2 + \frac{\tilde{y}'^2}{1 - \eta_k^2 \tau^2}\right)\right], \tag{12}$$

$$\alpha_{y'}(x', y') = \frac{1}{\pi D_d^2 \Sigma_{\text{crit}}} \int_0^1 \tau \, d\tau \sum_k \frac{M_k}{\sigma_k} \frac{\tilde{y}'}{\left(1 - \eta_k^2 \tau^2\right)^{3/2}}$$
$$\times \exp\left[-\frac{\tau^2}{2}\left(\tilde{x}'^2 + \frac{\tilde{y}'^2}{1 - \eta_k^2 \tau^2}\right)\right], \tag{13}$$

where both the deflection angle and the widths σ_k are expressed in radians; $\tilde{x}' \equiv x'/\sigma_k$ and $\tilde{y}' \equiv y'/\sigma_k$ are the sky coordinate (normalized to σ_k) with respect to the lens center. As before, $\eta_k^2 = (1 - q_k^2)$. The critical surface density

$$\Sigma_{\text{crit}} = \frac{c^2}{4\pi G} \frac{D_s}{D_{ds} D_d} \tag{14}$$

is the characteristic surface density used in gravitational lensing (e.g., Treu 2010).

5   MODELLING THE KINEMATICS

5.1   Predicting the observed second velocity moments with the anisotropic Jeans equations

Let us consider a steady-state axially symmetric stellar system characterized by a distribution function (DF) $f(\boldsymbol{x}, \boldsymbol{v})$, where the positions $\boldsymbol{x}$ and the velocities $\boldsymbol{v}$ are the phase-space coordinates, and subject to the influence of a total gravitational potential $\Phi_{\text{tot}}(R, z)$. While the typical observational data sets do not allow one, in general, to recover the full six-dimensional DF, it is possible to gain valuable information on the global dynamical structure of the system by noting that its velocity moments must satisfy the two Jeans equations (Binney & Tremaine 2008)

$$\frac{\partial(\rho\overline{v_z^2})}{\partial z} + \frac{1}{R}\frac{\partial(R\rho\overline{v_R v_z})}{\partial R} = -\rho\frac{\partial\Phi_{\text{tot}}}{\partial z} \tag{15}$$

$$\frac{\partial(\rho\overline{v_R^2})}{\partial R} + \frac{\partial(\rho\overline{v_R v_z})}{\partial z} = -\rho\frac{\partial\Phi_{\text{tot}}}{\partial R} + \rho\frac{\overline{v_\varphi^2} - \overline{v_R^2}}{R}. \tag{16}$$

Here, $\rho(R, z) \equiv \int f\,d^3\boldsymbol{v}$ denotes the three-dimensional density distribution of the stellar system, and the bar indicates a phase-space average of the quantity of interest, i.e.

$$\overline{v_i v_j} \equiv \frac{1}{\rho}\int v_i v_j f\,d^3\boldsymbol{v}. \tag{17}$$

The system is not required to be self-gravitating and therefore in Eqs (15) and (16) ρ might well be the density distribution ρ_{tr} of a tracer stellar component described by a DF f_{tr} and subject to an external potential. Moreover, if other collisionless components (each one defined by its own DF) are present, each one will obey its own set of Jeans equations *within the same total potential* Φ_{tot}.

In our dynamical analysis of late-type galaxies, we adopt an axisymmetric total potential $\Phi_{\text{tot}} = \Phi_\star + \Phi_{\text{DM}}$, where the two components represent the potentials of the luminous distribution and dark matter halo, respectively. We then write down and solve the Jeans equations, using the stellar density distribution $\rho_\star$ associated to the corresponding potential via the Poisson equation, in order to obtain the intrinsic velocity moments.[2] These are then projected along the line-of-sight and — after taking into account the effect

of instrumental PSF and aperture integration — compared with the corresponding observational quantities.

Of course, even when the potential and the density distributions are given, the two Equations (15) and (16) still depend on the four unknown functions $\overline{v_R^2}$, $\overline{v_\varphi^2}$, $\overline{v_z^2}$ and $\overline{v_R v_z}$, and therefore additional assumptions are needed in order to determine a unique solution for the Jeans equations. This is usually achieved by assigning the orientation and the shape of the intersection of the velocity dispersion ellipsoid with the meridional plane (R, z) at each point.

Observations of the Milky Way and of nearby disk galaxies show that the velocity dispersion ellipsoid is more flattened in the vertical direction than in the radial one[3], i.e. $\overline{v_z^2} < \overline{v_R^2}$ (see e.g. Wielen 1977, Gerssen, Kuijken, & Merrifield 1997, 2000, van der Kruit & de Grijs 1999, Shapiro, Gerssen, & van der Marel 2003, Ciardullo et al. 2004, Noordermeer, Merrifield, & Aragón-Salamanca 2008).

Cappellari (2008) introduced a simple and effective way (referred to as anisotropic Jeans models) to provide a closure for the Jeans equations that manages to reproduce this important feature. The two assumptions of this phenomenological model are: (i) the velocity dispersion ellipsoid is aligned with the cylindrical coordinate system (so that the mixed terms $\overline{v_R v_z}$ are everywhere zero) and (ii) the anisotropy in the meridional plane is constant, i.e. $\overline{v_R^2} = b\overline{v_z^2}$, with the anisotropy parameter $b \geqslant 0$. The meridional plane anisotropy is usually expressed in the literature using the parameter β_z, such that

$$\beta_z = 1 - \frac{\overline{v_z^2}}{\overline{v_R^2}} = 1 - \frac{1}{b}. \tag{18}$$

In real galaxies, the shape and the orientation of the velocity dispersion ellipsoid are in general a non-trivial function of the position on the meridional plane. However, the assumption of cylindrical alignment is quite accurate for fast-rotating galaxies and disk systems in general, in particular along the minor axis and, more crucially, in the vicinity of the equatorial plane, where the density is highest. In fact, Jeans models constructed with this simple prescription for the anisotropy have been shown to reproduce remarkably well the observed kinematic moments of fast rotators and spirals (Scott et al. 2009, Williams, Bureau, & Cappellari 2009).

With these assumptions, the Jeans Equations (15) and (16) become

$$\frac{\partial(\rho\overline{v_z^2})}{\partial z} = -\rho\frac{\partial\Phi_{\text{tot}}}{\partial z} \tag{19}$$

$$b\frac{\partial(\rho\overline{v_z^2})}{\partial R} = -\rho\frac{\partial\Phi_{\text{tot}}}{\partial R} + \rho\frac{\overline{v_\varphi^2} - b\overline{v_z^2}}{R}. \tag{20}$$

From the equations above, and imposing the intuitive constraint that the vertical pressure $\rho\overline{v_z^2} = 0$ for $z \to \infty$, one obtains the following expressions for the intrinsic second velocity moments along the coordinate directions:

$$\overline{v_z^2} = \frac{1}{\rho}\int_z^\infty \rho\frac{\partial\Phi_{\text{tot}}}{\partial z'}dz' \tag{21}$$

$$\overline{v_\varphi^2} = \frac{b}{\rho}R\frac{\partial\rho\overline{v_z^2}}{\partial R} + b\overline{v_z^2} + R\frac{\partial\Phi_{\text{tot}}}{\partial R}. \tag{22}$$

---

[2] Because of the collisionless nature of dark matter, one could write an analogous set of equations also for the halo component. However, since the corresponding velocity moments cannot be observed, this would be of no use in the present context of comparing the model predictions with the observed data sets.

[3] If the assumption of a steady-state axisymmetric system holds, this implies that the disk DF also depends on a third, non-classical, integral of motion I_3, in addition to the two classical integrals, namely the energy E and the angular momentum J_z along the rotation axis.

These intrinsic quantities are then integrated along the line of sight to obtain the projected second velocity moment $\overline{v_{los}^2}$ (whose square root is usually indicated as μ_2) which can be directly compared to the stellar kinematics observables. The projected velocity moments for the case of MGE parametrization are calculated in Cappellari (2008). The observational counterpart of the model quantity μ_2 is the root mean square velocity $v_{rms} \equiv \sqrt{v_{rot}^2 + \sigma^2}$, where v_{rot} and σ indicate the line of sight projected stellar rotation velocity and velocity dispersion, respectively.

We recall that, given a potential and a density distribution, the Jeans equations impose a condition for the equilibrium on the second velocity moments, but they provide no prescription on how to separate these moments into the contributions of random and ordered motions. Since no net radial or vertical motions are considered, and thus $\sigma_R^2 = \overline{v_R^2}$ and $\sigma_z^2 = \overline{v_z^2}$, here this issue would only be relevant for the splitting of the azimuthal component into the streaming motion $\overline{v_\varphi}$ and the velocity dispersion σ_φ, i.e. $\overline{v_\varphi^2} = \overline{v_\varphi}^2 + \sigma_\varphi^2$, which is usually tackled by adopting *ad hoc* assumptions such as the Satoh (1980) decomposition. In this work, however, we avoid making any additional assumptions in order to model $\overline{v_\varphi}$ separately, and we only model the second velocity moments as described above.

5.2 Predicting the observed gas circular velocity

In order to model the rotation curve of the Hα gas, we calculate the circular velocity profile, $v_c(R)$, of a test particle of negligible mass in a circular orbit in the equatorial plane of the galaxy.

The circular velocity, as it is clear from its definition, i.e. $v_c^2(R) = R(\partial\Phi_{tot}/\partial R)|_{z=0}$, is uniquely determined by the total gravitational potential of the galaxy. In general, v_c differs from the stellar rotation velocity $\overline{v_\varphi}$ (often referred to as streaming motion) which is usually lower due to the effect of the stellar velocity dispersion, which acts as a pressure term (see e.g. Binney & Tremaine 2008).

The (squared) circular velocity profile that corresponds to the MGE mass model described in Section 3 is readily calculated from Eqs (5)–(6) and has the following expression:

$$v_c^2(R) = 4\pi G R^2 \int_0^1 \tau^2 d\tau \sum_k \frac{q_k \rho_{0k}}{\sqrt{1 - \eta_k^2 \tau^2}} \exp\left(-\frac{\tau^2}{2\sigma_k^2}R^2\right), \qquad (23)$$

where again $\eta_k^2 = (1 - q_k^2)$ and the constant $\rho_{0k} \equiv \rho_k(0,0)$ is the central value of the mass density distribution of the k-th Gaussian element.

In order to compare the predicted rotation curve $v_c(R)$ of Eq. (23) with the observations, we also take into account the combined effects of inclination, PSF blurring and finite slit width, collectively referred to as beam-smearing. Since the exact distribution of the Hα gaseous component is not known from the observations, we approximate it using the available K'-band light profile instead, which is more accurate than using an exponential disk model. Additionally, in keeping with Paper II, we have cautionarily excluded from the fit two regions of the rotation curve: (i) the inner 2 arcsec, a region where the Hα distribution is probably asymmetric, due to the effect of extinction and (ii) the outermost three points of the west side of the rotation curve, which are affected by a spurious decrease of the velocity caused by the warp.

6 BAYESIAN INFERENCE AND UNCERTAINTIES

In order to derive rigorous constraints on the parameters that characterize the adopted model, we conduct our analysis within the standard framework of Bayesian statistics (see, e.g., MacKay 2003 and Sivia & Skilling 2006 for an extensive treatment of this subject).

Let us denote the combined data sets as d and the considered hypothesis as $\mathcal{H}(\theta)$. In our case, for instance, $\mathcal{H}$ includes the model that we have adopted to describe the mass distribution and dynamics of the galaxy under study (Sections 3–5), and also all the assumptions we make about the uncertainties on the data, instrument response functions and any prior knowledge of the situation we might want to include. The non-linear parameters θ may include, in general, not only the physical parameters η defining the total mass density distribution, but also the parameters that characterize the dynamics (e.g. anisotropy) and the geometry (e.g. inclination) of the system.

From Bayes' theorem, the posterior probability distribution function (PDF) for the set of parameters θ is given by

$$\Pr(\theta|d,\mathcal{H}) = \frac{\Pr(d|\theta,\mathcal{H})\Pr(\theta|\mathcal{H})}{\Pr(d|\mathcal{H})}, \qquad (24)$$

where $\Pr(d|\theta,\mathcal{H})$ is the likelihood, $\Pr(\theta|\mathcal{H})$ is the prior, and $\Pr(d|\mathcal{H})$, i.e. the factor required to normalize the posterior over θ, is known as the Bayesian evidence, which is used in comparing different model forms. When modelling the lensing and kinematic data we do not keep track of the value of the evidence, but do make use of it in Section 7.4 below.

The set of parameters θ_{MAP} for which the posterior is maximized identifies the *maximum a posteriori* (MAP) model. The MAP model can be interpreted as a "best model" of sorts, in the sense that it represents the combination of parameters that is found to best reproduce the data given our assumptions. We adopt it as our reference model for the times when we need to show our best estimates of the predicted observables (lensed image, rotation curve, velocity moments) and the reconstructed background lensed source.

The primary quantities of interest are the marginalized posterior PDFs for individual parameters θ_i obtained by integrating the joint posterior PDF over all the other parameters. These integrals can be performed most readily if we characterise the joint posterior by a set of sample parameter values drawn from it. The marginalised distributions are then readily approximated by histograms of these samples. When a more compact representation is required, we quote parameter constraints as the median values of these one-dimensional histograms, θ_{med}, and quantify our uncertainty with their 68% credible intervals (CIs, calculated by taking the 16th and 84th percentiles).

The model that we employ for the analysis of SDSS J2141 has six free parameters, i.e. parameters with uninformative priors which are allowed to vary and for which the posterior exploration is performed. These are: the virial velocity v_{vir}, the inner logarithmic slope γ, the concentration c_{-2} and the three-dimensional axial ratio q_h which describe the gNFW dark matter halo (Section 3.2); the global stellar mass-to-light ratio $\Upsilon_\star$ of the luminous component (Section 3.1), that is more readily interpreted when expressed in terms of the total stellar mass $M_\star \equiv \Upsilon_\star L_{tot}$; and the meridional plane anisotropy parameter b (Section 5.1). In analogy with Paper II, we adopt a broad Gaussian prior for v_{vir} centered on 255 km s^{-1} with a width of 45 km s^{-1}. This corresponds to the prior adopted in Paper II for the virial velocity of their non-singular
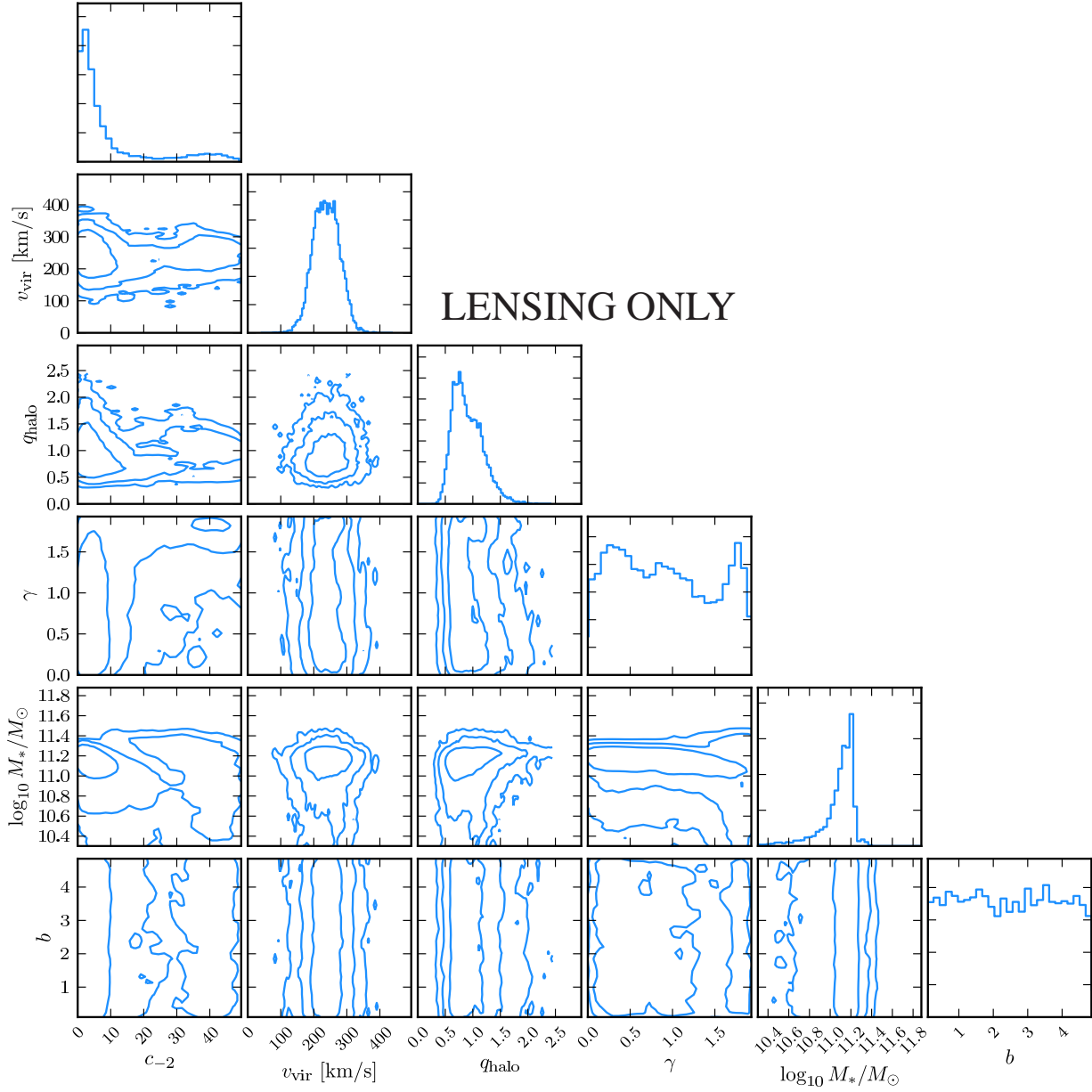
Figure 3. Marginalized two-dimensional (contour plots) and one-dimensional (histograms) posterior PDFs for the galaxy model parameters using constraints from the gravitational lensing data set only. The three contours indicate the regions containing, respectively, 68%, 95% and 99.7% of the probability.

isothermal halo, and is equivalent to assuming that the scale radius is not so large that the virial velocity is dramatically larger than the observed rotation velocity. We also adopt, as in Paper II, a lognormal prior centered on $q_h = 1$ (spherical) for the axial ratio, which allows for both oblate and prolate haloes. We let c_{-2} vary on a wide uniform prior from 0 to 50 to represent our ignorance of the halo concentration. The inner logarithmic slope γ is allowed to vary between 0 (flat core) and 2 (isothermal). We note that v_{vir} is allowed to go to zero, so that we are also including in our analysis the case of a disk galaxy with no dark matter halo, fully described by a self-gravitating stellar mass distribution. By letting the total stellar mass

vary (with uniform prior) between 0 and $5 \times 10^{11} M_\odot$ we allow for a wide range of contributions of the luminous components to the total mass, including the limiting case in which the galaxy is fully dark matter dominated and the stars are only a tracer with negligible mass. Finally, the anisotropy parameter can vary uniformly from $b = 0$, indicating a velocity dispersion ellipsoid without any radial component, to $b = 5$, for which the velocity dispersion ellipsoid is very elongated along the radial direction: this interval is wide enough to include all the values of meridional plane anisotropy observed in real disk galaxies (see Section 7.5). The model parameters, together with the adopted priors, are summarized in Table 1. A
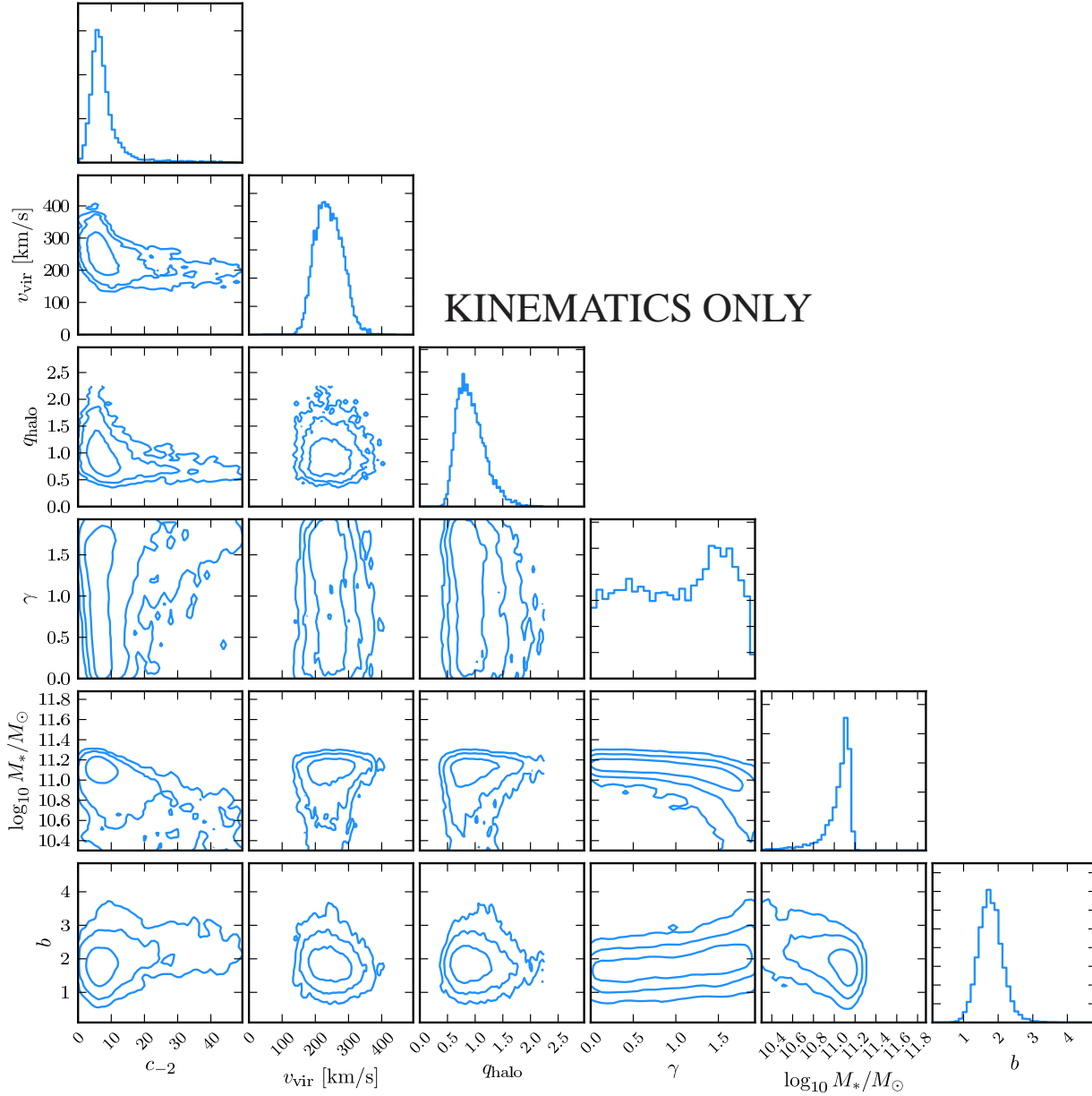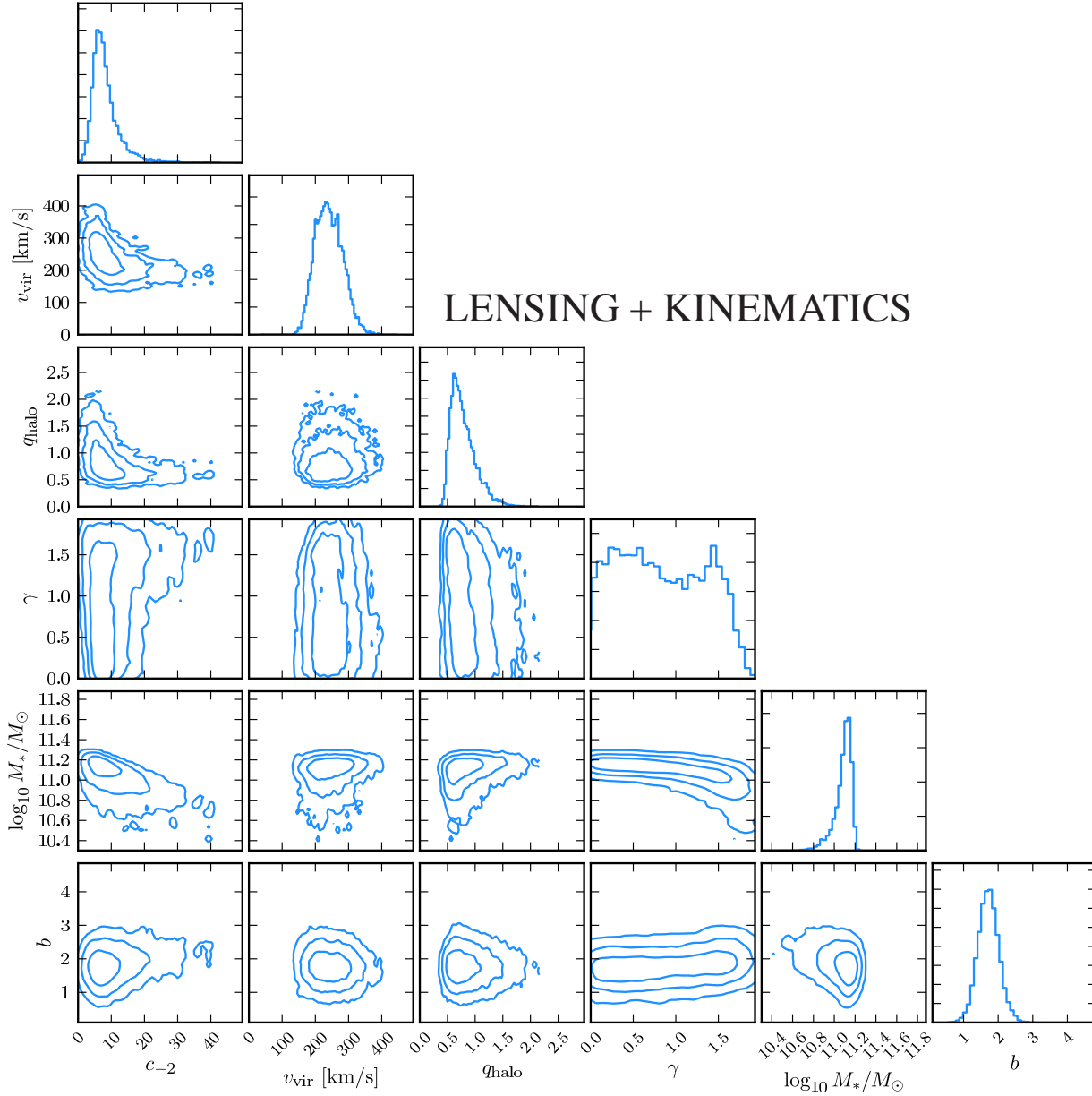
Figure 4. Marginalized two-dimensional (contour plots) and one-dimensional (histograms) posterior PDFs for the galaxy model parameters using constraints from the kinematics data set only. The three contours indicate the regions containing, respectively, 68%, 95% and 99.7% of the probability.

full description of the model also includes a number of additional parameters that do not represent physical characteristics of the system (i.e., the line-of-sight inclination, the lens center, the regularization level, the weights, widths and flattenings of the individual MGE Gaussians): these are treated as nuisance parameters and kept fixed or marginalized over.

For the likelihood function we follow the standard approach of assuming Gaussian errors on the data points (see e.g. Brewer & Lewis 2006; Suyu et al. 2006; Marshall et al. 2007). In

this case, the joint likelihood can be written simply as

$$
\Pr(\boldsymbol{d}\,|\,\boldsymbol{\theta}, \mathcal{H}) \propto \exp\left\{ -\frac{1}{2}\sum_{i=1}^{N_\ell} \frac{\left[\ell_i^{\mathrm{obs}} - \ell_i^{\mathrm{mod}}(\boldsymbol{\theta})\right]^2}{\sigma_{\ell,i}^2} \right.
$$
$$
\left. -\frac{1}{2}\sum_{i=1}^{N_{\mu_2}} \frac{\left[\mu_{2,i}^{\mathrm{obs}} - \mu_{2,i}^{\mathrm{mod}}(\boldsymbol{\theta})\right]^2}{\sigma_{\mu_2,i}^2} -\frac{1}{2}\sum_{i=1}^{N_{v_c}} \frac{\left[v_{c,i}^{\mathrm{obs}} - v_{c,i}^{\mathrm{mod}}(\boldsymbol{\theta})\right]^2}{\sigma_{v_c,i}^2} \right\}, \quad (25)
$$

where the three terms inside the exponential represent the familiar χ^2 misfit functions for the separate contributions of gravitational lensing, stellar kinematics and gas kinematics, respectively. We in-

Figure 5. Marginalized two-dimensional (contour plots) and one-dimensional (histograms) posterior PDFs for the galaxy model parameters using the combined constraints from both lensing and kinematics. The three contours indicate the regions containing, respectively, 68%, 95% and 99.7% of the probability.

dicate as $\ell_i^{\rm obs}$ the N_ℓ data points constituting the lensing data set, i.e. the pixel values in the galaxy-subtracted observed lensed image (see top-right panel of Figure 1), each characterized by an uncertainty $\sigma_{\ell,i}$. We denote as $\ell_i^{\rm mod}$ the corresponding pixel values of the model-predicted image, which are determined by the specific choice of model parameters $\boldsymbol{\theta}$ (for example, the bottom left panel of Figure 1 shows $\ell_i^{\rm mod}(\boldsymbol{\theta}_{\rm MAP})$, i.e. the model-predicted image in the case of the MAP model). An analogous notation (i.e., observed values, model-predicted values, uncertainties on the data points) applies for the velocity moment μ_2 in the case of the stellar kinematics and for the circular velocity $v_{\rm c}$ in the case of gas kinematics.

The computationally expensive task of exploring and sampling the joint posterior distribution is accomplished by making use of the very efficient and robust MULTINEST algorithm (Feroz & Hobson 2008; Feroz et al. 2009), which implements the nested sampling Monte Carlo technique (Skilling 2004; Sivia & Skilling 2006), and can provide reliable posterior inferences even in presence of multi-modal and degenerate multivariate distributions. For the analysis of SDSS J2141, we have launched MULTINEST with 2000 live points (the live or active points are the initial samples, drawn from the prior distribution, from which the posterior exploration is started). The large number of live

Table 1. Summary of the adopted priors and of the posteriors inferred from the combined analysis for the model parameters.

parameter	description	prior	posterior
$v_{\rm vir}/\,{\rm km\,s}^{-1}$	dark halo virial velocity	$\mathcal{N}(255, 45)$	242^{+44}_{-39}
γ	dark halo inner logarithmic slope	$U(0, 2)$	$0.82^{+0.65}_{-0.54}$
c_{-2}	dark halo concentration	$U(0, 50)$	$7.7^{+4.2}_{-2.5}$
$q_{\rm h}$	dark halo 3D axial ratio	$L\mathcal{N}(1, 0.3)$	$0.75^{+0.27}_{-0.16}$
$M_\star/10^{11}\,{\rm M}_\odot$	stellar mass	$U(0, 5)$	$1.32^{+0.16}_{-0.25}$
b	orbital anisotropy parameter: σ_R^2/σ_z^2	$U(0, 5)$	$1.77^{+0.30}_{-0.29}$

Note. In the prior column, $U(a, b)$ denotes a uniform distribution over the open interval (a, b); $\mathcal{N}(a, b)$ denotes a normal distribution, with a being the central value and b being the standard deviation; $L\mathcal{N}(a, b)$ denotes a lognormal distribution, with a being the central value for the variable, and b being the standard deviation for the log of the variable. In the posterior column, we list, for each parameter, the median value of the corresponding marginalized posterior PDF and the uncertainty quantified by taking the 68% credible interval (i.e., the 16th and 84th percentiles).

points adopted for this study (cf., e.g., the MULTINEST analysis in Barnabè et al. 2011) has allowed us not only to produce very detailed posterior distributions, but also to gauge the minimum number of live points (which is found to be ∼200) needed to obtain reliable posterior PDFs, which will be very useful in reducing the computational load in future analyses of further SWELLS systems.

7   RESULTS AND DISCUSSION

In this Section we present and discuss the results of our analysis of the disk galaxy SDSS J2141, combining the constraints from both the gravitational lensing and the kinematic data sets as described in the previous Sections.

7.1   Inferences on the galaxy model parameters

As discussed in Section 6, the inferences on the model parameters obtained from our analysis are expressed in the form of a multivariate posterior PDF. We consider six free parameters: the virial velocity $v_{\rm vir}$, inner logarithmic slope γ, concentration c_{-2} and three-dimensional axial ratio $q_{\rm h}$ of the gNFW dark matter halo, the total stellar mass $M_\star$, and the meridional plane orbital anisotropy ratio b. Since visualizing the full six-dimensional surface is challenging, we present the inferences in the familiar form of "cornerplots" that show all possible one-dimensional and two-dimensional marginalized posterior PDFs for the six model parameters. The inferences obtained when using just one single data set are presented in Figures 3 (gravitational lensing only) and 4 (kinematics only), while Figure 5 shows the results for the combined lensing and kinematics data sets. In each plot, the three contours indicate the regions containing, respectively, 68%, 95% and 99.7% of the probability, i.e. they represent the analogue of the 1, 2 and 3σ contours of a Gaussian distribution. The median value and the corresponding uncertainties (expressed as 16th and 84th percentiles) for each individual parameter are listed in Table 1.

The constraints provided by kinematics alone are in general slightly better than the constraints obtained with a pure gravitational lensing analysis, in particular for the concentration and the stellar mass; obviously, the anisotropy parameter b is completely unconstrained in the lensing analysis, and thus, in this case, the posterior is nothing else than the input uniform prior. The inferences on the remaining parameters have uncertainties of similar magnitude in the two cases, but the marginalized posterior PDFs have different shapes (note, in particular, the profile for the marginalized PDF of the halo axial ratio in the two cases), which makes it possible to tighten the inferences when lensing and kinematics data are considered simultaneously. The effectiveness of the combined analysis can be seen in Figure 5: in particular, we can place tight constraints on $M_\star$ by clipping both the low-mass and the high-mass tails, and we also improve significantly our inferences on the dark halo parameters $q_{\rm h}$ and γ, for which we weed out the higher values. The meaning and implications of the constraints on the model parameters are discussed below in Sections 7.2–7.5.

The high-probability models drawn from the posterior PDF of the combined analysis, and in particular the MAP model, reproduce both the lensing and the kinematic observables very accurately (Figures 1 and 2, respectively). Similarly to what was found in Paper II, the most probable lensing models predict a faint counterimage whose presence is consistent with the noise level. For the kinematics, we note that the predicted gas rotation curve matches quite well also the data points within the inner 2 arcsec, which were conservatively excluded from the fit.

7.2   Mass budget: baryons and dark matter

A very intuitive way to visualize the galaxy mass budget as a function of radius that is inferred from the combined analysis is provided by Figure 6, where we show the circular velocity profile obtained from the posterior PDF, decomposed into the baryonic and dark matter components. The solid lines indicate the median values from the posterior PDF, while the shaded regions represent the 68 per cent confidence intervals. The constraints on the total circular velocity $v_{\rm tot}$ are extremely tight, whereas there are larger uncertainties on the contributions given by the separate components. Despite this, it is clear that the baryonic matter is dominant all over the entire region for which we have data, with the dark matter component becoming progressively more important as we move outwards in radius.

Traditionally, in studies of disk galaxies, the characteristic radius at which one measures the dark matter fraction $f_{\rm DM} \equiv M_{\rm DM}/M_{\rm tot}$ is 2.2 times the disk scale length $R_{\rm d}$, which corresponds to the radius at which the circular speed peaks for a razor-thin exponential disk (see, e.g., Bershady et al. 2010 and references therein).
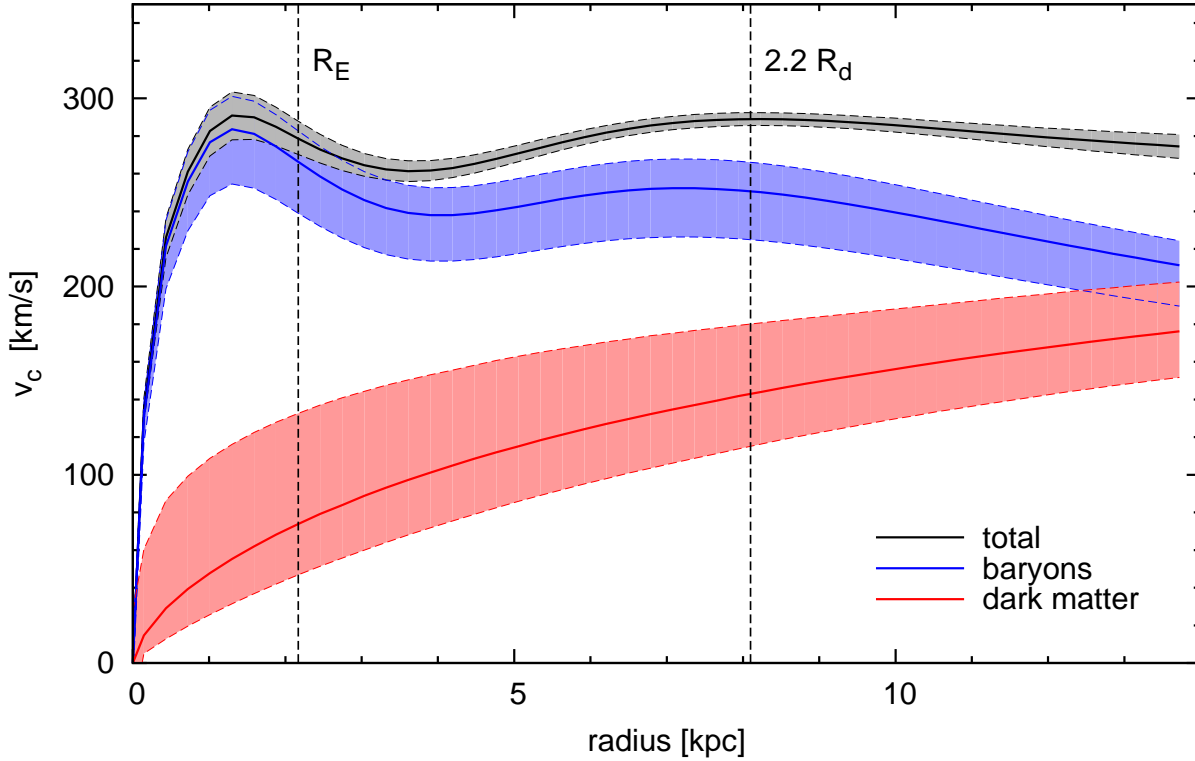
Figure 6. Circular velocity profile inferred from the combined lensing and dynamics analysis. The total circular velocity is shown in black, while the baryonic and dark matter components are plotted in blue and in red, respectively. For each component, the solid line represents the median while the shaded region encloses 68% of the posterior PDF. The two vertical dashed lines mark, for reference, the location of the Einstein radius R_E (left) and of $2.2R_d$ (right), where $R_d = 3.58$ kpc is the disk scale length of the galaxy.

In the case of SDSS J2141, we determine $f_{DM}(2.2R_d) = 0.28^{+0.15}_{-0.10}$, by integrating the mass within a spherical radius $r = 2.2R_d$. We note that this dark matter fraction was inferred from gravitational data alone, and is independent of the stellar populations in the galaxy. The marginalized posterior PDF for this quantity is shown in Figure 7: it is clear that the distribution peaks at around $f_{DM} \simeq 0.3$; dark matter dominated models (i.e. $f_{DM} > 0.5$), however, are still possible, albeit with a low probability of about 9 percent. Models without dark matter, on the other hand, are ruled out at more than the 3-sigma level, i.e. the probability for $f_{DM} < 0.05$ is less than 0.3 per cent. The Paper II analysis of this same galaxy — carried out using a less flexible mass model and without including the stellar kinematic constraints — found (at lower precision) a higher contribution of dark matter at $2.2R_d$, i.e. $f_{DM} = 0.55^{+0.20}_{-0.15}$, which is however still consistent within 1-sigma with the result that we determine here. Trott et al. (2010) and Suyu et al. (2011), by applying a combined lensing and dynamics analysis on two different disk galaxies, obtain a fractional amount of dark matter close to 45 ± 10 percent, which is slightly higher than (but not inconsistent with) the f_{DM} that we derive from the present analysis. On the other hand, van de Ven et al. (2010), by conducting a combined lensing and dynamics study of the same early-type disk galaxy studied by Trott et al. (2010), and adopting a Kroupa (2001) IMF, find that the upper limit for f_{DM} is only ≈ 0.20. Interestingly, the value of f_{DM} that we obtain in this analysis is similar to the typical average dark matter fraction of about 30 per cent determined for massive early-type galaxies within one effective radius based on lensing and dynamical analysis (e.g., Treu & Koopmans 2004; Treu et al. 2010; Auger et al. 2010b; Spiniello et al. 2011), or by assuming maximal

stellar component (e.g., Gerhard et al. 2001, Cappellari et al. 2006, Barnabè et al. 2010, 2011). However, one should keep in mind that f_{DM} has been observed to vary quite significantly between individual systems.

This analysis also enables us to test whether the "maximum disk" hypothesis (van Albada & Sancisi 1986), frequently adopted in studies of late-type galaxies (e.g. Bell & de Jong 2001), holds for the object examined here. We follow the definition of maximum disk introduced by Sackett (1997), i.e. $v_{disk}(2.2R_d)/v_{tot}(2.2R_d) = 0.85 \pm 0.10$, substituting the circular velocity of the disk v_{disk} with the more relevant circular velocity of the entire baryonic component, v_{bar}. We find that $v_{bar}(2.2R_d)/v_{tot}(2.2R_d) = 0.87^{+0.05}_{-0.09}$, which corresponds to a maximal disk. From the posterior PDF for this ratio, the probability that the SDSS J2141 disk is submaximal is about 10 per cent.

This result would make SDSS J2141 something of an outlier when compared with a sample, recently studied using dynamical methods, of 30 local disk galaxies (Bershady et al. 2011; Martinsson 2011). These authors find that, although the ratio $v_{disk}(2.2R_d)/v_{tot}(2.2R_d)$ increases with the maximum rotation speed of the galaxy, even the most massive systems with $v_{disk}(2.2R_d) \gtrsim 250$ km s^{-1} are submaximal on average. We note, however, that the existence of individual massive galaxies consistent with "maximal-ity" is not ruled out in their study (see, in Figure 2 of Bershady et al. 2011, the outlier and the error bars for some of the highest rotation velocity systems). In addition, it is important to keep mind that both our method and that of Bershady et al. (2011) inevitably rely on different assumptions: in our case, for example, a common mass-to-light ratio for bulge and disk, in their case assumptions necessary

to compare edge-on and face-on galaxies. In addition, the methods obtain their information from different parts of the mass distribution, with our method being more sensitive to the inner regions, owing to the lensing and stellar velocity dispersion constraints. We plan to perform a more detailed comparison of the two results once data and models for the full SWELLS sample will be available.

7.3 Constraints on the dark matter halo: shape and profile

Pure dark matter N-body simulations find that dark halos generally have triaxial shapes, with a preference for prolateness, particularly in the inner regions (e.g Jing & Suto 2002; Allgood et al. 2006; Bett et al. 2007; Macciò et al. 2008). Recent numerical work (see, e.g., Abadi et al. 2010; Tissera et al. 2010) has shown that including the contribution of the baryons has the effect of modifying the overall profile of the dark halo, which flattens to a more axisymmetric and oblate shape, with an average axial ratio of order $0.85 - 0.95$, largely constant with radius. In our study of SDSS J2141, we infer from the combined analysis that the dark halo is moderately oblate, with an axial ratio $q_h = 0.75^{+0.27}_{-0.16}$. Significantly prolate haloes with $q_h > 1.25$ are strongly disfavoured (i.e., with less than 5 per cent probability). This is in good agreement with the numerical results on baryon-affected halos, although the median value is slightly flatter than the typical q_h obtained in the simulations. The axial ratio obtained for SDSS J2141 in Paper II (using a less flexible NIE dark halo model which does not allow for a variable inner slope), i.e. $q_h = 0.91^{+0.15}_{-0.13}$, was closer to spherical but still consistent, within the 68% uncertainty, with the more accurate analysis conducted here. In contrast, in the only other joint lensing and kinematics study of a disk galaxy that adopts a non-spherical halo model, Suyu et al. (2011) find a much more flattened dark matter distribution, with $q_h = 0.33$. These authors adopt a simpler luminous mass model than the one considered here (i.e., a razor-thin exponential disk and a point-mass bulge) and do not have access to stellar kinematics data.

Including the inner slope γ as a free parameter in the dark halo mass density model (see Section 3.2), rather than just adopting a fixed isothermal or NFW profile (as done in previous studies, cf. Paper II and Suyu et al. 2011; but see also Trott et al. 2010, where a spherical gNFW halo is used), is important since it allows one to account for possible baryon-induced effects, such as adiabatic contraction, that can modify the steepness of the density distribution in the galaxy central regions. The data-set at hand, unfortunately, does not permit us to place a strong constraint on the inner slope: we obtain $\gamma = 0.82^{+0.65}_{-0.54}$, approximately equiprobable over the range 0 to 1.5, and perfectly consistent with an unmodified NFW profile. The probability that the halo has an inner slope $1.5 \leqslant \gamma < 2$ is 14 per cent. We are able to conclude, however, that very steep profiles are disfavoured: slopes $1.7 \leqslant \gamma < 2$ have only a 3.5 per cent probability, whereas from the adopted uniform prior U(0,2) (see Table 1) one would predict 15 per cent over the same interval.

We infer a halo concentration parameter $c_{-2} = 7.7^{+4.2}_{-2.5}$, with a low-probability tail for high concentrations (the 95th and 98th percentiles fall at $c_{-2} \simeq 17$ and $c_{-2} \simeq 30$, respectively). The inferred virial velocity is $v_{vir} = 242^{+44}_{-39}$. From these parameters one can derive the posterior PDFs for all other useful quantities characterizing the gNFW halo, such as the generalized scale radius $r_{-2} = 41^{+27}_{-19}$ kpc, the virial radius $r_{vir} = 315^{+57}_{-53}$ kpc and the virial mass $\log_{10}(M_{vir}/M_\odot) = 12.48^{+0.28}_{-0.27}$.

Figure 8 shows a comparison between the dark matter concentration and the virial velocity from our lensing and dynamics analysis of SDSS J2141 (contours), with the predictions from N-body
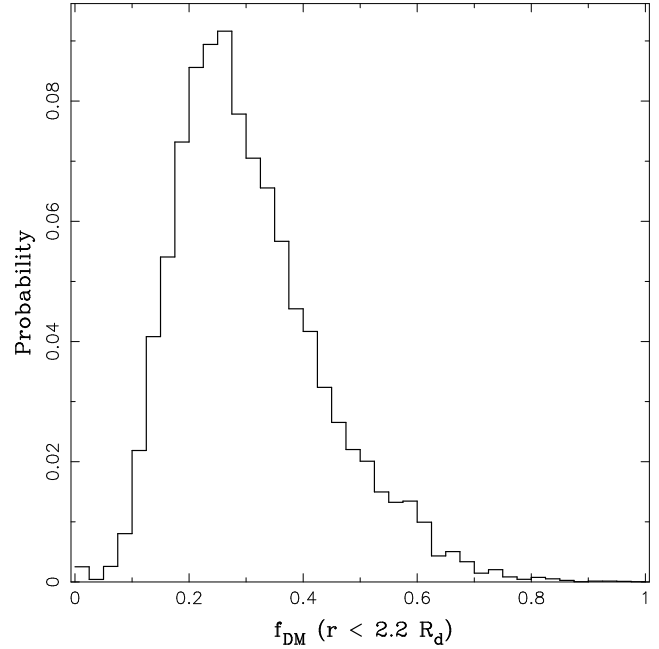

Figure 7. Dark matter fraction enclosed within the spherical radius $r = 2.2$ disk scale lengths, inferred from the combined lensing and dynamics analysis. The median and uncertainty (corresponding to 16th and 84th percentiles) is $f_{DM} = 0.28^{+0.15}_{-0.10}$.

simulations in a WMAP 5th year cosmology (Macciò et al. 2008). The uncertainty on our inferred dark matter concentration is quite broad $\simeq 0.2$ dex, but is nevertheless in very good agreement with the simplest predictions from ΛCDM (i.e., assuming no contraction or expansion of the dark matter in response to galaxy formation).

7.4 Constraints on the stellar IMF

The total stellar mass inferred from the combined lensing and dynamics analysis is $\log_{10}(M_\star/M_\odot) = 11.12^{+0.05}_{-0.09}$. This value is very well constrained and represents a significant improvement over the $M_\star$ determination of Paper II, by cutting the low mass tail of the posterior PDF of about 0.3 dex.

In order to draw conclusions on the galaxy IMF, we need to compare the stellar mass derived from the joint analysis with the stellar masses that are inferred from SPS models when assuming either a Chabrier (2003) or a Salpeter (1955) IMF. The SPS analysis is performed by applying the Auger et al. (2009) code on the multi-band photometric data set of SDSS J2141, as described in Paper II. However, we note that so far we have neglected the contribution of the cold gas: if such a component is present, the mass $M_\star$ derived above from the combined analysis actually represents the total *baryonic* mass. Therefore, in order to obtain a posterior PDF for the stellar mass that can be properly compared with the predictions from the SPS models, we need to subtract the cold gas fraction, which in disk galaxies (with stellar masses of $M_\star \simeq 10^{11} M_\odot$) accounts for about 20 ± 10 per cent of the baryonic mass (see e.g. Dutton & van den Bosch 2009). Under the assumption that the cold gas is distributed approximately like the stars, for each sample in the posterior PDF of $M_\star$ we draw a random gas fraction $f_{gas} \in [0, 1]$ from a Gaussian distribution centered on 0.2 with a standard deviation of 0.1, and we calculate the quantity $M_\star(1 - f_{gas})$. The gas-subtracted stellar mass derived in this way is $\log_{10}(M_\star/M_\odot) = 11.01^{+0.08}_{-0.11}$, about 0.1 dex lower than the value
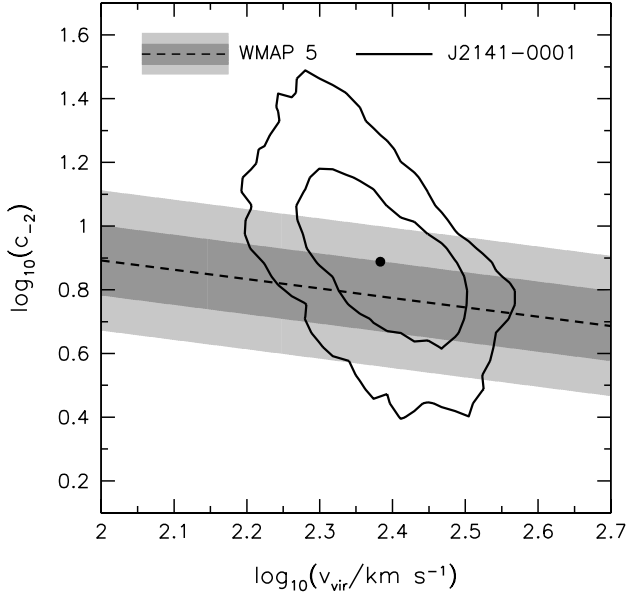
Figure 8. Dark matter concentration $c_{-2} \equiv r_{vir}/r_{-2}$ vs dark matter virial velocity v_{vir}. The shaded region shows the prediction (with 1- and 2-sigma scatter) from N-body simulations in a WMAP 5th year ΛCDM cosmology (Macciò et al. 2008). The contours enclose 68% and 95% of the posterior probability from the combined lensing and dynamics analysis. The black dot shows the median of the posterior distribution.

obtained above by ignoring the cold gas contribution. This provides a robust lower bound to the stellar mass function. In the future, it will be useful to refine these mass estimates by including high resolution constraints on the gas fraction from ALMA observations.

The posterior PDF for the inferred stellar mass (both with and without cold gas) is presented in Figure 9, and compared with the distributions obtained for a Chabrier and Salpeter IMF. It is clear, just by a visual inspection of this Figure, that our results support a Chabrier-like IMF over a Salpeter one. This preference can be quantified in a rigorous way by calculating the Bayes factor, i.e. the evidence ratio between the two models

$$B_{CS} = \frac{\int \mathcal{L}(M_\star) \Pr(M_\star \mid \mathcal{H}_C) \, dM_\star}{\int \mathcal{L}(M_\star) \Pr(M_\star \mid \mathcal{H}_S) \, dM_\star}, \qquad (26)$$

where in our case the likelihood $\mathcal{L}(M_\star)$ is the posterior PDF for the inferred stellar mass, while the priors $\Pr(M_\star \mid \mathcal{H}_C)$ and $\Pr(M_\star \mid \mathcal{H}_S)$ are given by the posterior PDFs obtained from SPS models in the cases of Chabrier and Salpeter IMFs, respectively. The calculated Bayes factor is $B_{CS} = 5.7$, which corresponds to substantial evidence in favour of a Chabrier IMF with respect to a Salpeter IMF (see e.g. Kass & Raftery 1995, and references therein). In other words, if these are the only two possible models, this value of B_{CS} means that there is a 85 per cent probability that the Chabrier model is the true one.

This result corroborates the findings of Paper II, and is in agreement with the works of, e.g, Bell & de Jong (2001), Kassin et al. (2006) and van de Ven et al. (2010), which disfavour a Salpeter IMF for disk galaxies, preferring instead IMFs that predict lower stellar masses, such as Chabrier or Kroupa (2001). Low-mass, fast-rotating early-type galaxies are also found to be often inconsistent with a Salpeter IMF (e.g. Cappellari et al. 2006; Auger et al. 2010a; Barnabè et al. 2010). On

the other hand, there is mounting evidence that massive ellipticals favour a Salpeter-like (Auger et al. 2010b; Treu et al. 2010; Barnabè et al. 2011; Spiniello et al. 2011) or an even steeper IMF (van Dokkum & Conroy 2010). These findings, including the results of this work, support the idea that the traditional picture of a universal IMF (see, e.g., Kroupa 2002) might need to be revised in favour of a more complicated scenario where the IMF depends on the galaxy mass and/or Hubble type.

7.5 Constraints on the stellar anisotropy

Determining the shape of the velocity dispersion ellipsoid of disk galaxies is important not only in order to understand their global dynamical properties, which are related to the formation and evolution mechanisms, but also because the vertical-to-radial velocity dispersion ratio σ_z/σ_R can be used, together with the galaxy scale height distribution, to derive the dynamical mass of the disk (see e.g. Bottema 1997; Kregel et al. 2005; Westfall et al. 2011).

From our analysis, we infer a meridional anisotropy parameter $b = 1.77^{+0.30}_{-0.29}$, with a very symmetric posterior distribution around the median value. In order to facilitate the comparison with the disk galaxy studies literature, it is convenient to express the anisotropy in the notation $\beta_z = 1 - \sigma_z^2/\sigma_R^2$ (see Sect. 5.1), where $\beta_z = 0$ corresponds to isotropy: in this case we have $\beta_z = 0.43^{+0.08}_{-0.11}$. These results show that, for SDSS J2141, the velocity dispersion in the vertical direction is about three quarters of the radial velocity dispersion. The probability that the velocity dispersion ellipsoid is approximately isotropic in the meridional plane (i.e., $\beta_z = 0.0 \pm 0.1$) is only of order 1 per cent. This confirms that two-integral DF models (which are semi-isotropic, i.e. have $\sigma_R^2 = \sigma_z^2$ everywhere, see e.g. Binney & Tremaine 2008) do not provide an ideal description of the dynamical properties of this galaxy, and a more flexible approach allowing for anisotropy, such as the one adopted in this work, is warranted. Within the hypothesis of axial symmetry, we can then conclude that the disk galaxy DF respects a third integral of motion (cf., e.g., Noordermeer et al. 2008).

These findings are in agreement with numerous dynamical studies of disk galaxies, including the Milky Way, which are well known to have velocity dispersion ellipsoids flattened along the vertical direction (see van der Kruit & Freeman 2011, and references therein). For local disk galaxies, Gerssen et al. (1997, 2000) and Shapiro et al. (2003) determine $0.30 \lesssim \beta_z \lesssim 0.75$. Williams et al. (2009), adopting a dynamical model analogous to the one used in this work (i.e., based on anisotropic Jeans equations), find $0.0 \lesssim \beta_z \lesssim 0.5$ for a sample of 14 spiral and S0 galaxies. Noordermeer et al. (2008), using two-dimensional kinematic data sets to analyze the dynamics of four early-type disk galaxies, find $\beta_z \simeq 0.5$, perfectly consistent with the result for SDSS J2141. Recently, one of the galaxies studied in detail in the DiskMass Survey was determined to have a more flattened $\beta_z = 0.77$ (Westfall et al. 2011).

We remark that the present study represents the first determination of the anisotropy parameter for a disk galaxy well beyond the local Universe, at a redshift $z_{lens} \simeq 0.14$ (a previous combined lensing and dynamics study of a disk galaxy at a lower redshift, $z_{lens} \simeq 0.04$, was conducted by van de Ven et al. 2010, who found $\beta_z = 0.1 \pm 0.1$, consistent with the system being semi-isotropic).
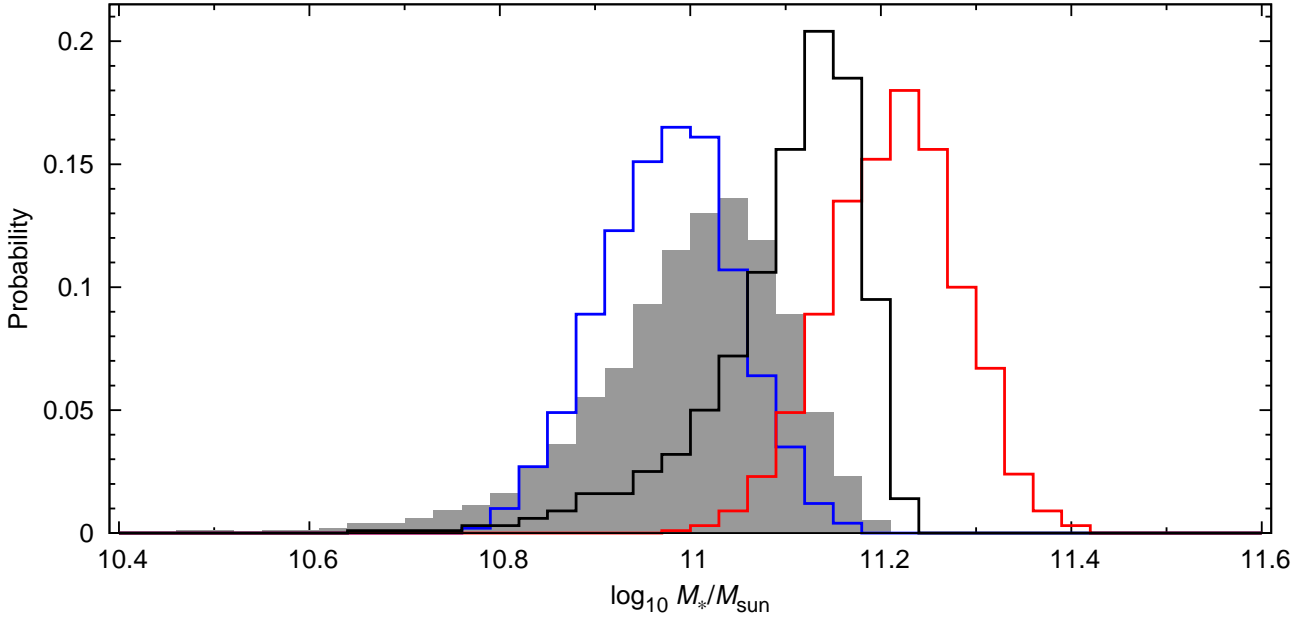
Figure 9. Comparison of the stellar mass inferred from the combined lensing and dynamics analysis (black) with the stellar mass determined from photometry and stellar population synthesis models, assuming a Chabrier IMF (blue) or a Salpeter IMF (red). The grey shaded histogram shows the posterior PDF for the inferred stellar mass when a 20% ± 10% contribution in mass from cold gas in included. In the latter case, the Bayes factor in favor of a Chabrier IMF with respect to the Salpeter IMF is 5.7, corresponding to Chabrier being preferred at 85%.

8   CONCLUSIONS

We have carried out an in-depth, self-consistent analysis of the mass and dynamical structure of the lens disk galaxy SDSS J2141 at redshift 0.14 by combining the constraints from gravitational lensing, $H\alpha$ rotation curve and stellar kinematics. We have adopted a flexible axially symmetric mass model consisting of a gNFW dark matter halo and a self-gravitating stellar distribution obtained from the MGE parametrization of the observed luminous profile. We have modelled the kinematics by means of anisotropic Jeans equations in order to allow for a velocity dispersion ellipsoid that is flattened in the meridional plane, as is typical for disk galaxies.

This work improves in several ways (namely, the inclusion of stellar kinematics constraints and the upgraded mass and dynamical model) on the study of this same object described in Paper II, and represents the most accurate and detailed analysis to date of the dark and luminous mass profile of a disk galaxy beyond the local Universe, i.e. at redshift $\gtrsim 0.1$. The main conclusions of this analysis can be summarized as follows:

(i) The spherical dark matter mass fraction within $2.2R_d$ is $f_{DM} = 0.28^{+0.15}_{-0.10}$, independent of assumptions on the stellar populations in the galaxy. The dark matter fraction increases with radius, but does not become dominant within the range probed by the observations, which extend to approximately $R = 14$ kpc. Models without dark matter (i.e., $f_{DM} < 0.05$) are ruled out at more than the 3-sigma level.

(ii) We test the maximum disk hypothesis: we find that, at $2.2R_d$, the fractional contribution of the baryons to the total circular velocity is $0.87^{+0.05}_{-0.09}$. This corresponds to a maximal disk (following the definition of Sackett 1997); the probability of having a submaximal disk for SDSS J2141 is 10 per cent. This is in disagreement with recent studies of local disk galaxies (e.g., the DiskMass Sur-

vey, Bershady et al. 2011, Martinsson 2011), which typically find submaximal disks.

(iii) The gNFW dark matter halo is characterized by a virial velocity $v_{vir} = 242^{+44}_{-39}$ km s^{-1} and a concentration parameter $c_{-2} = 7.7^{+4.2}_{-2.5}$, implying a generalized scale radius $r_{-2} = 41^{+27}_{-19}$ kpc. This is in very good agreement with the predictions from N-body simulations in a ΛCDM cosmology (i.e., assuming no contraction or expansion of the halo in response to galaxy formation).

(iv) The inner slope of the dark matter halo is only weakly constrained, $\gamma = 0.82^{+0.65}_{-0.54}$, and is consistent with an unmodified NFW profile ($\gamma = 1$). We can still conclude, however, that very steep inner profiles with $\gamma \gtrsim 1.7$ are disfavoured.

(v) The dark matter halo is moderately oblate, with a three-dimensional axial ratio $q_h = 0.75^{+0.27}_{-0.16}$, and a very low probability for significantly prolate haloes (i.e., $q_h \gtrsim 1.25$). Recent high-resolution simulations (e.g. Abadi et al. 2010; Tissera et al. 2010) find that the baryons have the effect of turning the prolate triaxial dark matter halos into roughly oblate spheroids, a scenario that is consistent with the results of this work.

(vi) The total baryonic mass is tightly constrained by the combined lensing and dynamics analysis, and is determined to be $\log_{10}(M_\star/M_\odot) = 11.12^{+0.05}_{-0.09}$, independent of the IMF. When accounting for the expected cold gas contribution, we obtain a stellar mass $\log_{10}(M_\star/M_\odot) = 11.01^{+0.08}_{-0.11}$. This value is in excellent agreement with the stellar mass that is predicted when assuming a Chabrier IMF. Model comparison shows that there is substantial evidence in favour of a Chabrier IMF with respect to a Salpeter IMF (the Bayes factor is 5.7, corresponding to a 85 per cent probability).

(vii) We infer a meridional anisotropy parameter $\beta_z = 0.43^{+0.08}_{-0.11}$, implying that, for SDSS J2141, the velocity dispersion ellipsoid in the meridional plane is flattened along the vertical direction, in agreement with most studies of local disk galaxies. Semi-isotropic models (i.e., $\beta_z \approx 0$) are ruled out at a very high confidence level,

corroborating the evidence that the dynamics of disk galaxies is not adequately described by two-integral DFs, and a third integral of motion is required.

REFERENCES

Abadi, M. G., Navarro, J. F., Fardal, M., Babul, A., & Steinmetz, M. 2010, MNRAS, 407, 435

Allgood, B., Flores, R. A., Primack, J. R., Kravtsov, A. V., Wechsler, R. H., Faltenbacher, A., & Bullock, J. S. 2006, MNRAS, 367, 1781

Auger, M. W., Treu, T., Bolton, A. S., Gavazzi, R., Koopmans, L. V. E., Marshall, P. J., Bundy, K., & Moustakas, L. A. 2009, ApJ, 705, 1099

Auger, M. W., Treu, T., Bolton, A. S., Gavazzi, R., Koopmans, L. V. E., Marshall, P. J., Moustakas, L. A., & Burles, S. 2010a, ApJ, 724, 511

Auger, M. W., Treu, T., Gavazzi, R., Bolton, A. S., Koopmans, L. V. E., & Marshall, P. J. 2010b, ApJ, 721, L163

Barnabè, M., Auger, M. W., Treu, T., Koopmans, L. V. E., Bolton, A. S., Czoske, O., & Gavazzi, R. 2010, MNRAS, 406, 2339

Barnabè, M., Czoske, O., Koopmans, L. V. E., Treu, T., & Bolton, A. S. 2011, MNRAS, 415, 2215

Barnabè, M., Czoske, O., Koopmans, L. V. E., Treu, T., Bolton, A. S., & Gavazzi, R. 2009a, MNRAS, 399, 21

Barnabè, M., & Koopmans, L. V. E. 2007, ApJ, 666, 726

Barnabè, M., Nipoti, C., Koopmans, L. V. E., Vegetti, S., & Ciotti, L. 2009b, MNRAS, 393, 1114

Bell, E. F., & de Jong, R. S. 2001, ApJ, 550, 212

Bendinelli, O. 1991, ApJ, 366, 599

Bershady, M. A., Martinsson, T. P. K., Verheijen, M. A. W., Westfall, K. B., Andersen, D. R., & Swaters, R. A. 2011, ApJ, 739, L47

Bershady, M. A., Verheijen, M. A. W., Westfall, K. B., Andersen, D. R., Swaters, R. A., & Martinsson, T. 2010, ApJ, 716, 234

Bett, P., Eke, V., Frenk, C. S., Jenkins, A., Helly, J., & Navarro, J. 2007, MNRAS, 376, 215

Binney, J., & Tremaine, S. 2008, Galactic Dynamics: Second Edition (Princeton University Press)

Blumenthal, G. R., Faber, S. M., Flores, R., & Primack, J. R. 1986, ApJ, 301, 27

Bolton, A. S., Burles, S., Koopmans, L. V. E., Treu, T., Gavazzi, R., Moustakas, L. A., Wayth, R., & Schlegel, D. J. 2008, ApJ, 682, 964

Bolton, A. S., Burles, S., Koopmans, L. V. E., Treu, T., & Moustakas, L. A. 2006, ApJ, 638, 703

Bottema, R. 1997, A&A, 328, 517

Brewer, B. J., & Lewis, G. F. 2006, ApJ, 637, 608

Cappellari, M. 2002, MNRAS, 333, 400

—. 2008, MNRAS, 390, 71

Cappellari, M., et al. 2006, MNRAS, 366, 1126

Chabrier, G. 2003, PASP, 115, 763

Chandrasekhar, S. 1969, Ellipsoidal Figures of Equilibrium (Yale University Press)

Ciardullo, R., Durrell, P. R., Laychak, M. B., Herrmann, K. A., Moody, K., Jacoby, G. H., & Feldmeier, J. J. 2004, ApJ, 614, 167

Czoske, O., Barnabè, M., Koopmans, L. V. E., Treu, T., & Bolton, A. S. 2008, MNRAS, 384, 987

—. 2012, MNRAS, 419, 656

Dekel, A., Devor, J., & Hetzroni, G. 2003, MNRAS, 341, 326

Dutton, A. A., Courteau, S., de Jong, R., & Carignan, C. 2005, ApJ, 619, 218

Dutton, A. A., & van den Bosch, F. C. 2009, MNRAS, 396, 141

Dutton, A. A., et al. 2011a, MNRAS, 416, 322

—. 2011b, MNRAS, 417, 1621

Emsellem, E., Dejonghe, H., & Bacon, R. 1999, MNRAS, 303, 495

Emsellem, E., Monnet, G., & Bacon, R. 1994, A&A, 285, 723

Feroz, F., & Hobson, M. P. 2008, MNRAS, 384, 449

Feroz, F., Hobson, M. P., & Bridges, M. 2009, MNRAS, 398, 1601

Gerhard, O., Kronawitter, A., Saglia, R. P., & Bender, R. 2001, AJ, 121, 1936

Gerssen, J., Kuijken, K., & Merrifield, M. R. 1997, MNRAS, 288, 618

—. 2000, MNRAS, 317, 545

Gnedin, O. Y., Kravtsov, A. V., Klypin, A. A., & Nagai, D. 2004, ApJ, 616, 16

Grillo, C., Gobat, R., Rosati, P., & Lombardi, M. 2008, A&A, 477, L25

Jiang, G., & Kochanek, C. S. 2007, ApJ, 671, 1568

Jing, Y. P., & Suto, Y. 2002, ApJ, 574, 538

Kass, R. E., & Raftery, A. E. 1995, J. Amer. Statistical Assoc., 90, 773

Kassin, S. A., de Jong, R. S., & Weiner, B. J. 2006, ApJ, 643, 804

Keeton, C. R. 2001, arXiv:astro-ph/0102341

Keeton, C. R., & Kochanek, C. S. 1998, ApJ, 495, 157

Kelson, D. D. 2003, PASP, 115, 688

Koopmans, L. V. E. 2005, MNRAS, 363, 1136

Koopmans, L. V. E., de Bruyn, A. G., & Jackson, N. 1998, MN-RAS, 295, 534

Koopmans, L. V. E., et al. 2009, ApJ, 703, L51

Kormann, R., Schneider, P., & Bartelmann, M. 1994, A&A, 284, 285

Kregel, M., van der Kruit, P. C., & Freeman, K. C. 2005, MNRAS, 358, 503

Kroupa, P. 2001, MNRAS, 322, 231

—. 2002, Science, 295, 82

Macciò, A. V., Dutton, A. A., & van den Bosch, F. C. 2008, MN-RAS, 391, 1940

MacKay, D. J. C. 2003, Information Theory, Inference and Learning Algorithms (Cambridge University Press)

Maller, A. H., Simard, L., Guhathakurta, P., Hjorth, J., Jaunsen, A. O., Flores, R. A., & Primack, J. R. 2000, ApJ, 533, 194

Marshall, P. J., et al. 2007, ApJ, 671, 1196

Martinsson, T. P. K. 2011, PhD thesis, University of Groningen

Monnet, G., Bacon, R., & Emsellem, E. 1992, A&A, 253, 366

Navarro, J. F., Frenk, C. S., & White, S. D. M. 1997, ApJ, 490, 493

Nipoti, C., Treu, T., Ciotti, L., & Stiavelli, M. 2004, MNRAS, 355, 1119

Noordermeer, E., Merrifield, M. R., & Aragón-Salamanca, A. 2008, MNRAS, 388, 1381

Rybicki, G. B. 1987, in IAU Symposium, Vol. 127, Structure and Dynamics of Elliptical Galaxies, ed. P. T. de Zeeuw, 397

Sackett, P. D. 1997, ApJ, 483, 103

Salpeter, E. E. 1955, ApJ, 121, 161

Satoh, C. 1980, PASJ, 32, 41

Schneider, P., Kochanek, C. S., & Wambsganss, J. 2006, Gravitational Lensing: Strong, Weak and Micro, Saas-Fee Advanced Courses, 33 (Berlin, Springer-Verlag)

Scott, N., et al. 2009, MNRAS, 398, 1835

Sérsic, J. L. 1968, Atlas de galaxias australes (Cordoba, Argentina: Observatorio Astronomico)

Shapiro, K. L., Gerssen, J., & van der Marel, R. P. 2003, AJ, 126, 2707

Sivia, D. S., & Skilling, J. 2006, Data Analysis: A Bayesian Tutorial (Oxford University Press)

Skilling, J. 2004, in American Institute of Physics Conference Series, Vol. 735, American Institute of Physics Conference Series, ed. R. Fischer, R. Preuss, & U. V. Toussaint, 395–405

Spiniello, C., Koopmans, L. V. E., Trager, S. C., Czoske, O., & Treu, T. 2011, arXiv:astro-ph/1103.4773

Suyu, S. H., Marshall, P. J., Hobson, M. P., & Blandford, R. D. 2006, MNRAS, 371, 983

Suyu, S. H., et al. 2011, ArXiv: astro-ph/1110.2536

Tissera, P. B., White, S. D. M., Pedrosa, S., & Scannapieco, C. 2010, MNRAS, 406, 922

Treu, T. 2010, ARAA, 48, 87

Treu, T., Auger, M. W., Koopmans, L. V. E., Gavazzi, R., Marshall, P. J., & Bolton, A. S. 2010, ApJ, 709, 1195

Treu, T., Dutton, A. A., Auger, M. W., Marshall, P. J., Bolton,

A. S., Brewer, B. J., Koo, D. C., & Koopmans, L. V. E. 2011, MNRAS, 417, 1601

Treu, T., & Koopmans, L. V. E. 2002, ApJ, 575, 87

—. 2004, ApJ, 611, 739

Trott, C. M., Treu, T., Koopmans, L. V. E., & Webster, R. L. 2010, MNRAS, 401, 1540

van Albada, T. S., & Sancisi, R. 1986, Royal Society of London Philosophical Transactions Series A, 320, 447

van de Ven, G., Falcón-Barroso, J., McDermid, R. M., Cappellari, M., Miller, B. W., & de Zeeuw, P. T. 2010, ApJ, 719, 1481

van der Kruit, P. C., & de Grijs, R. 1999, A&A, 352, 129

van der Kruit, P. C., & Freeman, K. C. 2011, ARAA, 49, 301

van der Kruit, P. C., & Searle, L. 1981, A&A, 95, 105

van Dokkum, P. G., & Conroy, C. 2010, Nature, 468, 940

Warren, S. J., & Dye, S. 2003, ApJ, 590, 673

Weijmans, A.-M., Krajnović, D., van de Ven, G., Oosterloo, T. A., Morganti, R., & de Zeeuw, P. T. 2008, MNRAS, 383, 1343

Westfall, K. B., Bershady, M. A., Verheijen, M. A. W., Andersen, D. R., Martinsson, T. P. K., Swaters, R. A., & Schechtman-Rook, A. 2011, ApJ, 742, 18

Wielen, R. 1977, A&A, 60, 263

Williams, M. J., Bureau, M., & Cappellari, M. 2009, MNRAS, 400, 1665

Wyithe, J. S. B., Turner, E. L., & Spergel, D. N. 2001, ApJ, 555, 504

Zhao, H. 1996, MNRAS, 278, 488